Title

Torque- and Muscle-Driven Flexion Induce Disparate Risks of In Vitro Herniation: A Multiscale and Multiphasic Structure-Based Finite Element Study.

Journal

Journal of Biomechanical Engineering, 144(6)

ISSN

0148-0731

Authors

Zhou, Minhao
Huff, Reece D
Abubakr, Yousuf
et al.

Publication Date

2022-06-01

DOI

10.1115/1.4053402

Peer reviewed

Torque- and Muscle-Driven Flexion Induce Disparate Risk of *In Vitro* Herniation: A Multiscale and Multiphasic Structure-Based Finite Element Study

Minhao Zhou
University of California, Berkeley
Mechanical Engineering Department
2162 Etcheverry Hall, #1740
Berkeley, CA 94720-1740
minhao.zhou@berkeley.edu

Reece D. Huff
University of California, Berkeley
Mechanical Engineering Department
2162 Etcheverry Hall, #1740
Berkeley, CA 94720-1740
rdhuff@berkeley.edu

Yousuf Abubakr
University of California, Berkeley
Mechanical Engineering Department
2162 Etcheverry Hall, #1740
Berkeley, CA 94720-1740
yousufabubakr123@berkeley.edu

Grace D. O'Connell[1]
University of California, Berkeley
Mechanical Engineering Department
University of California, San Francisco
Orthopaedic Surgery Department
2162 Etcheverry Hall, #1740
Berkeley, CA 94720-1740
g.oconnell@berkeley.edu

[1] Corresponding author: Grace D. O'Connell – g.oconnell@berkeley.edu

ABSTRACT

The intervertebral disc is a complex structure that experiences multiaxial stresses regularly. Disc failure through herniation is a common cause of lower back pain, which causes reduced mobility and debilitating pain, resulting in heavy socioeconomic burdens. Unfortunately, herniation etiology is not well understood, partially due to challenges in replicating herniation in vitro. Previous studies suggest that flexion elevated risks of herniation. Thus, the objective of this study was to use a multiscale and multiphasic finite element model to evaluate the risk of failure under torque- or muscle-driven flexion. Models were developed to represent torque-driven flexion with the instantaneous center of rotation (ICR) located on the disc, and the more physiologically representative muscle-driven flexion with the ICR located anterior of the disc. Model predictions highlighted disparate disc mechanics regarding bulk deformation, stress-bearing mechanisms, and intradiscal stress-strain distributions. Specifically, failure was predicted to initiate at the bone-disc boundary under torque-driven flexion, which may explain why endplate junction failure, instead of herniation, has been the more common failure mode observed in vitro. By contrast, failure was predicted to initiate in the posterolateral annulus fibrosus under muscle-driven flexion, resulting in consistent herniation. Our findings also suggested that muscle-driven flexion combined with axial compression could be sufficient for provoking herniation in vitro and in silico. In conclusion, this study provided a computational framework for designing in vitro testing protocols that can advance the assessment of disc failure behavior and the performance of engineered disc implants.

[1] Corresponding author: Grace D. O'Connell – g.oconnell@berkeley.edu

1. Introduction

In vitro tissue mechanical testing is essential for understanding the *in vivo* structure-function relationship of the human lumbar spine under different mechanical stimuli and for evaluating the effect of disease and their corresponding clinical interventions. However, the clinical relevance of most *in vitro* tests and their capability in accurately predicting *in vivo* mechanical or biological response greatly depends on the study design and testing protocols, which can introduce unexpected artifacts into the measured data and subsequent conclusions [Costi et al., 2021]. For example, variables such as specimen geometry, buffer solution, loading rate, and compressive preload have all been shown to alter mechanical properties at the tissue- or joint-level [Schmidt et al., 2016; Safa et al., 2017; Werbner et al., 2017, 2019, 2021; Newell et al., 2020]. Thus, caution is needed when designing *in vitro* testing protocols or interpreting the relative clinical impact of data collected from *in vitro* experiments.

Mechanical failure of the intervertebral disc, including disc herniation, is a common cause of lower back pain and can affect 10% of the population annually [Yao, et al., 2020]. Disc herniation involves the protrusion or extrusion of disc materials beyond the intervertebral disc boundaries and has been the most common cause of sciatica, which causes decreased mobility and debilitating pain, resulting in large socioeconomic burdens [Katz 2006; Schroeder et al., 2016]. Lumbar disc herniation has been the focus of spinal biomechanical and clinical research since the early 20th century [Truumees 2015]. However, despite significant developments in intervertebral disc joint-level testing techniques over the last 70 years, challenges remain in repeatably inducing herniation *in*

[1] Corresponding author: Grace D. O'Connell – g.oconnell@berkeley.edu

vitro, largely due to difficulties in recreating the multiaxial loads that the disc experience during physiological activities [Wilke et al., 2016].

The range of viable lumbar disc *in vitro* mechanical tests and their clinical relevance are often limited by the capabilities of available testing equipment. For example, *in vivo* flexion and extension motions are mainly driven by active physiological structures (*e.g.*, muscles), causing the instantaneous center of rotation (ICR) to be located at some distance away from the disc (*i.e.*, muscle-driven) [White and Panjabi, 1990]. However, *in vitro* flexion or extension testing of lumbar motion segments or functional units has been primarily conducted with the ICR located within the disc boundary, limited by torque-driven mechanical testers [Wilke et al., 2016]. Non-physiological torque-driven flexion or extension tests could contribute to the limited success in provoking herniation *in vitro*, making it more challenging for researchers to study the etiology and progression of disc herniation. For example, Adams and Hutton attempted to induce herniation by loading joint-level specimens under axial compression with a flexion angle. However, 70-83% of the samples experienced non-herniation failure, with at least 40% of them experiencing endplate junction failure [Adams and Hutton, 1983a, b; Adams and Hutton, 1985]. More recently, studies using 6-degree-of-freedom dynamic loading devices highlighted the benefit and necessity of applying combined multiaxial loadings to provoke *in vitro* herniation. However, ~50% of the lumbar motion segment specimens were still excluded due to endplate failure [Wilke et al., 2016; Berger-Roscher et al., 2017].

Finite element models have been an effective tool for complementing experimental studies, providing predictions of tissue mechanical responses that are

[1] Corresponding author: Grace D. O'Connell – g.oconnell@berkeley.edu

difficult or impossible to measure in the laboratory. Previously, researchers have used various models of the lumbar intervertebral discs to investigate joint-level mechanics and tissue-level stress and strain distributions. However, many of these models rely on single-phasic or poroelastic material descriptions that are not capable of describing Donnan equilibrium [Shirazi-Adl et al., 1984; Kurowski and Kubo, 1986; Kim et al., 1991; Shirazi-Adl 1992; Rohlmann et al., 2006; Schmidt et al., 2007a, b; Galbusera et al., 2011a, b; Barthelemy et al., 2016; Castro and Alves, 2021]. Donnan equilibrium is largely responsible for the active swelling behavior in biological tissues, playing a pivotal role in tissue mechanics [Ehlers et al., 2009].

To address these limitations, we recently developed and validated a novel structure-based triphasic model for the bovine caudal motion segment. Model parameters were determined based on known physical or biochemical properties reported in the literature (*e.g.*, collagen fiber stiffness, fixed charge density) [Zhou et al., 2021a]. The model accurately predicted disc mechanics across the joint, tissue, and subtissue scales and helped elucidate important load-bearing mechanisms between tissue phases (*e.g.*, between fluid and solid phases) or tissue subcomponents (*e.g.,* between fibers and the extrafibrillar matrix), which are essential for understanding and assessing disc failure behavior under multiaxial mechanical loading.

In this study, we aimed to employ our validated multiscale multiphasic structure-based model to address the current challenges in replicating physiological loading and disc failure *in vitro*. The objective of this study was twofold. The first objective was to investigate disc mechanics under both torque- and muscle-driven flexion. The second

[1] Corresponding author: Grace D. O'Connell – g.oconnell@berkeley.edu

objective was to relate those findings to observations of clinical and experimental disc failure by assessing the risk of herniation under torque- and muscle driven flexion. Although the current model was developed from bovine caudal disc geometry, the results highlight disparate disc mechanical behavior, including stress and strain concentrations that correspond to clinical observations for bulging or herniated discs under muscle-driven flexion. Moreover, model predictions under torque-driven flexion highlighted strain concentrations that correspond to disc failure modes commonly observed *in vitro* for human and ovine discs. Thus, the findings from this study are considered translatable to relevant human disc biomechanics research.

2. Methods

2.1. Model development

Finite element models of the bovine caudal disc motion segment were created based on our previous work (**Figure 1A**) [Zhou et al., 2021a]. To replicate motion segment samples prepared for most *in vitro* experiments, posterior structures, including facets joints and ligaments, were not included. The model geometry was created in Solidworks (Solidworks 2020). Finite element meshes were generated using ABAQUS and ANSA pre-processor (Abaqus 6.14; ANSA 15.2.0). The appropriate mesh size was determined using results from our previous mesh convergence study [Zhou et al., 2021b]. Boundary and loading conditions were defined in FEBioStudio, and the fully developed models were solved by FEBio (FEBioStudio 1.5) [Maas et al., 2012]. Our prior work validated that proportional scaling did not significantly alter model predictions [Zhou et al., 2021a]. Thus, the disc joint was modeled at a 1:5 scale (~2.1 million tetrahedral elements) for

[1] Corresponding author: Grace D. O'Connell – g.oconnell@berkeley.edu

computational efficiency due to limited accessible computing power (maximum of ~200 million nonzero entries in the stiffness matrix can be evaluated).

Model geometry was determined based on data in the literature. A circular cross section was assumed in the transverse anatomical plane. Disc radius and height (not including bony endplates) were 2.85 and 1.40 mm, respectively (**Figure 1A**) [O'Connell et al., 2007a]. The nucleus pulposus (NP) was assumed to have the same circular cross section, with a ~50% smaller radius (1.45 mm; **Figure 1A**) [O'Connell et al., 2007a]. The annulus fibrosus (AF) was created using the multiscale structure-based modeling approach validated in our previous work [Zhou et al., 2020, 2021a]. Particularly, seven concentric 0.2 mm-thick lamellae were modeled as fiber-reinforced angle-ply composites containing distinct materials for fiber bundles and the extrafibrillar matrix that occupy separate volumes (**Figure 1A**) [Adam et al., 2015]. Native bovine AF structural features, including lamellar thickness, fiber bundle radius, and interfibrillar spacing, were maintained during the downscale to reduce the total number of elements required. This scaling approach has been widely applied and validated in human disc finite element models [Shirazi-Adl et al., 1984; Goel et al., 1995a; Galbusera et al., 2011a, b], and has been shown to improve computational efficiency while maintaining fiber volume fraction and preserving mesh quality for model convergence [Zhou et al., 2021b]. AF fiber bundles were modeled as uniformly distributed, full-length cylinders welded to the surrounding matrix [Goel et al., 1995a; Michalek et al., 2009; Schollum et al., 2010]. Although available data regarding bovine AF structure are limited in the literature, similarities between human and bovine AF structures have been reported [Yu et al., 2007]. Therefore, fiber

[1] Corresponding author: Grace D. O'Connell – g.oconnell@berkeley.edu

bundle geometry from the human AF was applied, where fiber bundle radius was 0.06 mm and interfibrillar spacing within each lamella was 0.22 mm [Marchand and Ahmed, 1990]. Fibers were oriented at ±45° to the transverse plane in the inner AF and decreased along the radial direction to ±30° in the outer AF (**Figure 1A** – bottom right inset; **Figure 1B** – turquoise circles) [Matcher et al., 2004]. Cartilage endplates (CEP) covered the superior and inferior ends of the NP and the inner-to-mid AF (**Figure 1A** – cartilage endplate); spatial variations in CEP thickness were also incorporated (**Figure 1A** – top inset) [Berg-Johansen et al., 2018]. Bony endplates were modeled to cover both the superior and inferior ends of the disc (**Figure 1A** – bony endplate). All interfaces were defined as welded interfaces [Adam et al., 2015]. To exclude the effect of mesh size on model-predicted mechanics, element size was held constant for the NP, AF, and CEP across all models.

Triphasic mixture theory was employed to account for Donnan equilibrium to properly describe the tissue water content and osmotic response [Lai et al., 1991]. The Holmes-Mow description was applied to model the strain-dependent tissue permeability (k) of the NP, AF, and CEP (**Equation 1**), where J was the determinant of the deformation gradient tensor (***F***), k_0 represented hydraulic permeability in the reference configuration, φ_0 represented tissue solid volume fraction, and M represented the exponential strain-dependence coefficient.

$$k(J) = k_0 \left(\frac{J-\varphi_0}{1-\varphi_0}\right)^2 e^{\frac{1}{2}M(J^2-1)} \qquad \textbf{(1)}$$

Fixed charge density represented the proteoglycan content in the NP, CEP, and AF extrafibrillar matrix, driving the osmotic response. Radial variation in fixed charge density

[1] Corresponding author: Grace D. O'Connell – g.oconnell@berkeley.edu

and AF solid volume fraction were determined based on previous literature and our recent work, where high-spatial-resolution measurements of bovine caudal disc biochemical composition were provided (**Figure 1B** – grayscale circles; **Figure 1C**) [Beckstein et al., 2008; Bezci et al., 2019]. Collagen fiber bundles were assumed to have no active swelling capacity (*i.e.*, zero fixed charge density). Free diffusivity (D_0) and within-tissue diffusivity (D) terms for Na^+ and Cl^- ions for the simulated phosphate-buffered saline solution were set based on data from Gu et al. [2004] with a 100% ion solubility assumed ($D_{0,Na^+} = 0.00116$ mm^2/s; $D_{0,Cl^-} = 0.00161$ mm^2/s; $D_{Na^+} = 0.00044$ mm^2/s; $D_{Cl^-} = 0.00069$ mm^2/s). The solution osmotic coefficient (0.927) was determined based on a linear interpolation of data reported in Partanen et al. [2017].

A compressible hyperelastic Holmes-Mow material description was used to describe NP, CEP, and AF extrafibrillar matrix mechanics (**Equations 2-4**) [Cortes et al., 2014]. In the equations, I_1 and I_2 represented the first and second invariants of the right Cauchy-Green deformation tensor, $\boldsymbol{C}$ ($\boldsymbol{C} = \boldsymbol{F}^T\boldsymbol{F}$), E represented Young's modulus, ν represented Poisson's ratio, and β represented the exponential stiffening coefficient. AF collagen fibers were modeled using the same compressible hyperelastic Holmes-Mow as the ground matrix but were reinforced with a tension-only power-linear fiber description to account for AF nonlinearity and anisotropy (**Equation 5**). In **Equation 5**, γ represented the power-law exponent in the toe region, E_{lin} represented the fiber modulus in the linear region, and λ_0 represented the transitional stretch between the toe and linear regions. Additionally, B was a function of γ, $E_{lin.}$, and λ_0 ($B = \frac{E_{lin}}{2}(\frac{(\lambda_0{}^2-1)}{2(\gamma-1)} + \lambda_0{}^2)$.

[1] Corresponding author: Grace D. O'Connell – g.oconnell@berkeley.edu

Collagen fiber properties were determined based on uniaxial tensile data for type I collagen [Van der Rijt et al., 2006; Shen et al., 2008].

$$W(I_1, I_2, J) = \frac{1}{2}c(e^{Q} - 1) \quad \textbf{(2)}$$

$$Q = \frac{\beta(1+\nu)(1-2\nu)}{E(1-\nu)}\left[\left(\frac{E}{1+\nu} - \frac{E\,\nu}{(1+\nu)(1-2\nu)}\right)(I_1 - 3) + \frac{E\,\nu}{(1+\nu)(1-2\nu)}(I_2 - 3) - \left(\frac{E}{1+\nu} + \frac{E\,\nu}{(1+\nu)(1-2\nu)}\right) lnJ^2\right] \quad \textbf{(3)}$$

$$c = \frac{E(1-\nu)}{2\beta(1+\nu)(1-2\nu)} \quad \textbf{(4)}$$

$$\psi_n(\lambda_n) = \begin{cases} 0 & \lambda_n < 1 \\ \frac{E_{lin}}{4\gamma(\gamma-1)}({\lambda_0}^2 - 1)^{2-\gamma}(\lambda_n - 1)^{\gamma} & 1 \le \lambda_n \le \lambda_0 \\ E_{lin}(\lambda_n - \lambda_0) + B({\lambda_n}^2 - {\lambda_0}^2) + \frac{E_{lin}}{4\gamma(\gamma-1)}({\lambda_0}^2 - 1)^{2-\gamma}(\lambda_n - 1)^{\gamma} & \lambda_n > \lambda_0 \end{cases} \quad \textbf{(5)}$$

Bony endplates were modeled using a compressible hyperelastic material with the Neo-Hookean description (**Equation 6**). I_1, I_2, J were defined as above. $E_{bony\ endplates}$ and $\nu_{bony\ endplates}$ represented the Young's modulus (12,000 MPa) and Poisson's ratio (0.3), based on reported data in the literature [Choi et al., 1990; Goel et al., 1995b].

$$W_{bony\ endplates}(I_1, I_2, J) = \frac{E_{bony\ endplates}}{4(1+\nu_{bony\ endplates})}(I_1 - 3) - \frac{E_{bony\ endplates}}{2(1+\nu_{bony\ endplates})} lnJ + \frac{E_{bony\ endplates}\,\nu_{bony\ endplates}}{(1+\nu_{bony\ endplates})(1-2\nu_{bony\ endplates})}(lnJ)^2 \quad \textbf{(6)}$$

All model parameters were directly obtained from our previous work that developed and validated the model for the bovine caudal disc motion segment (**Supplementary Table 1**) [Zhou et al., 2021a]. Bovine tissue properties were used when corresponding data were available. When bovine data were not available, matching human disc properties were used, as previous studies have shown similarities between

[1] Corresponding author: Grace D. O'Connell – g.oconnell@berkeley.edu

healthy human and bovine disc mechanical and biochemical properties (**Supplementary Table 1** – "*") [Demers et al., 2004; Alini et al., 2008; Bezci et al., 2019].

2.2. Loading and boundary conditions

All models were loaded in three steps (**Figure 2A**). First, free swelling in the 0.15 M phosphate-buffered solution was applied until equilibrium. Then, a 0.5 MPa of axial compression was applied, which was immediately followed by a 5° flexion. During axial compression and flexion, all degrees of freedom were fixed for the bottom bony endplate (**Figure 2A** – fixed boundary condition). The flexion angle was determined based on human lumbar spine range of motion data [White and Panjabi, 1990]. Due to the symmetry in bovine caudal disc geometry, only flexion was simulated.

To model torque-driven flexion, the instantaneous center of rotation (ICR) was located on the line of symmetry on the top bony endplate (not including the edge; **Figure 3A**). For muscle-driven flexion, ICRs were located on the same line of symmetry but at some distance anterior of the disc edge (**Figure 3B**). A total of 10 cases were investigated, where Cases ***A*** to ***C*** were considered as torque-driven and Cases ***D*** to ***J*** were considered as muscle-driven (**Figure 3C**). The distance between the center of the top bony endplate and the ICR was defined as ICR distance (**Figure 3** – ICR distance). To examine the effect of flexion on initiating disc herniation, axial rotation was not included to avoid potential confounding effects. All models were simulated using steady-state analyses and the model output were evaluated at equilibrium.

2.3. Data analysis: Disc mechanics under torque- and muscle-driven flexion

[1] Corresponding author: Grace D. O'Connell – g.oconnell@berkeley.edu

The magnitude of the torque and corresponding force required to achieve 5° flexion were calculated. Force magnitudes were calculated as the torque divided by the corresponding ICR distance, which served as the lever arm. Intradiscal deformation was assessed by evaluating strains in the z-direction (**Figure 2B**), which represented changes in disc height, and AF bulging at mid-disc height (**Figure 2C** – solid red circles). The average disc height was calculated as the average of anterior and posterior disc height after flexion. Absolute AF bulging (*i.e.*, AF radial displacement after flexion, [mm]) and relative AF bulging (*i.e.*, [AF radial displacement post-flexion]/ [inner or outer radius of the AF ring]$\times 100\%$) were evaluated using the post-swelling configuration as the reference configuration to better mimic the reference configuration used for previous experimental studies [O’Connell et al., 2007b]. AF buckling was noted when the AF radius at mid-disc height became smaller than it was near the endplates.

Average disc solid stress (*i.e.*, stress taken by the tissue phase) and fluid pressure (*i.e.*, stress taken by the tissue fluid phase) were evaluated before and after flexion. The relative contribution of solid stress and fluid pressure was evaluated by normalizing each term by the total stress, which was defined as the sum of the two terms [Lai et al., 1991]. The effective Lagrangian strain, effective solid Lagrangian stress, fluid pressure, and maximum shear Lagrangian strain distributions were evaluated at the mid-frontal plane. Within the FEBio environment, effective stresses and strains are comparable to Von Mises stresses and strains. Average NP fluid pressure was also evaluated.

2.4. Data analysis: Predicting risk of herniation

[1] Corresponding author: Grace D. O’Connell – g.oconnell@berkeley.edu

Model predictions of *in vitro* disc herniation were determined using two failure criteria based on both the AF effective strain and AF fiber stretch [Schmidt et al., 2007a, b; Werbner et al., 2017]. We evaluated the risk of *in vitro* herniation mainly based on AF failure mechanics due to the clinical prevalence of AF failure in the posterolateral disc region, the availability of AF failure mechanics data in the literature, and the lack of failure mechanics data characterized at the disc-bone interface. The average effective strain values were calculated in the posterolateral inner and outer AF before and after the applied flexion (**Figure 2B** – Inner and outer AF; **Figure 2C** – Posterolateral region) and were compared to the effective failure strain threshold reported in the literature [Werbner et al., 2017]. Particularly, the range of effective strain that initiated failure in the AF was defined as 0.4 to 0.6, and the percentage of failed elements after flexion was calculated as the number of AF elements with an effective strain value above the threshold (*i.e.*, 0.5, calculated as the average of the upper and lower bound for the failure initiation range previously defined) divided by the total number of AF elements in the respective region. Due to the consistent mesh size defined, the failed element percentage was considered equivalent to failed tissue volume. The average AF fiber stretch in the posterolateral inner and outer AF with the corresponding percentage of failed elements was similarly calculated. The AF fiber stretch failure threshold (failure initiation range: 1.15-1.25; the failed element percentage was calculated using the fiber stretch value of 1.20) was determined based on values reported in previous joint-level studies [Schmidt et al., 2007a, b; Heuer et al., 2008].

[1] Corresponding author: Grace D. O’Connell – g.oconnell@berkeley.edu

AF maximum shear strain has been a commonly used metric to characterize disc mechanical response under combined loading in joint-level models [Schmidt et al., 2007a, b; Amin et al., 2019]. To examine maximum shear strain as a candidate for a failure criterion, the average maximum shear strain in the posterolateral inner and outer AF with the corresponding failed element percentage was calculated. The threshold (failure initiation range: 0.3-0.5; the failed element percentage was calculated using the maximum shear strain value of 0.4) was determined based on values reported in previous joint-level modeling studies [Schmidt et al., 2007a, b; Amin et al., 2019].

Although the risk of herniation *in vitro* was mainly evaluated using AF-based failure criteria, the average effective strain was evaluated at the rim (*i.e.*, outer cartilage endplate locating at the bone-AF interface) in the posterolateral region to help investigate the causes for the commonly observed endplate junction failure *in vitro* (**Figure 2C** – Posterolateral region; Rim). The range of effective strain that initiated failure in the rim was defined as 0.5 to 0.7, and the percentage of failed elements was calculated using the effective strain value of 0.6 [Danso et al., 2014].

3. Results

3.1. Disc mechanics under torque- and muscle-driven flexion

The torque magnitude required to achieve 5° flexion increased nonlinearly as the ICR distance increased, except for Case ***A***, whose ICR was located at the center of the top bony endplate (**Figure 4** – black circles). However, the corresponding force magnitude required followed a parabolic trend, reaching the minimum with an ICR distance between 3 and 6 mm, which was in the range of muscle-driven flexion (**Figure 4** – red circles).

[1] Corresponding author: Grace D. O’Connell – g.oconnell@berkeley.edu

The average disc height was maintained under torque-driven flexion but was increased under muscle-driven flexion (**Figure 5A** – gray circles). Specifically, under torque-driven flexion, the posterior AF experienced tensile strains while the anterior AF experienced compressive strains in the z-direction (**Figure 5A** – diagonal circles). However, under muscle-driven flexion, both the posterior and anterior sides of the disc experienced tensile z-strains (**Figure 5A** – solid circles). Overall, both the anterior and posterior disc height increased linearly with ICR distance, resulting in large disc height differences between torque- and muscle-driven cases (**Figure 5A**). For example, the average disc height for Case ***I*** (height: 2.2 mm) was ~50% greater than that for Case ***A*** (1.4 mm; **Figure 5B**).

The inner and outer radius of the AF ring were 1.56 and 2.94 mm in the reference configuration (**Figure 6A**). Assessment of AF radial displacement at the mid-disc height suggested outward bulging for both the inner and outer AF after compression (**Figure 6B**). Under torque-driven flexion, both the inner and outer AF bulged outward on the posterior side, while the anterior AF experienced inward bulging (**Figure 6C** – diagonal triangles and circles; **Figure 6D** – Cases ***A*** and ***B***). Under muscle-driven flexion, the relative inward bulging for the posterior AF and anterior outer AF increased with ICR distance (**Figure 6C** – solid orange circles and triangles; solid blue circles); however, bulging in the anterior inner AF was relatively consistent across all muscle-driven cases, ranging from -2.3% to -3.5% (**Figure 6C** – solid blue triangles). Buckling in the posterior outer AF was first observed in Case ***I***, when the relative inward bulging exceeded 4% (**Figure 6D** – Cases ***I***). Buckling in the anterior AF was not observed for any cases investigated.

[1] Corresponding author: Grace D. O'Connell – g.oconnell@berkeley.edu

Fluid pressure contributed significantly to the disc's overall stress-bearing capability. Before flexion was applied, the average fluid pressure was 0.24 MPa, which corresponded to 47% of the total stress (**Figure 7**). As the ICR distance increased, the average fluid pressure decreased nonlinearly from 0.25 MPa in Case ***A*** to 0.08 MPa in Case ***J*** (**Figure 7A** – blue bars), while the average solid stress followed a parabolic trend, reaching its minimum in Case ***F*** (0.11 MPa) and then increasing with ICR distance, reaching its maximum in Case ***J*** (0.43 MPa; **Figure 7A** – black bars). As a result, under torque-driven flexion, the relative solid stress and fluid pressure contributions were comparable and not altered by the applied flexion (**Figure 7B** – diagonal bars). However, under muscle-driven flexion, the relative fluid pressure contribution decreased pseudo-linearly with increasing ICR distance, from 55% in Case ***D*** to 15% in Case ***J*** (**Figure 7B** – solid bars).

Before flexion, high maximum shear strains and effective strains were observed near the rim (**Figure 8A**, **B** – "*"). The solid stress was mainly absorbed by the AF (**Figure 8C**), while the fluid pressure was concentrated in the NP, with an average NP fluid pressure of 0.47 MPa (**Figure 8D**). Torque-driven flexion had a minimal impact on maximum shear strain, effective strain, and fluid pressure distributions (**Figure 8A**, **B**, **D**) but resulted in greater stresses concentrated in the anterior outer AF (**Figure 8C**). By contrast, muscle-driven flexion resulted in higher maximum shear strains, effective strains, and effective solid stresses in the posterior AF and at the disc-bone boundary (**Figure 8A**-**C**). Additionally, the NP fluid pressure decreased pseudo-linearly with increasing ICR distance (**Figure 8D**; **Figure 8E** – solid black circles). For example, the average NP fluid pressure for Case ***I*** was 0.19 MPa, representing a 60% decrease from

[1] Corresponding author: Grace D. O'Connell – g.oconnell@berkeley.edu

Case ***A*** (0.47 MPa) and the pre-flexion configuration (0.47 MPa). Overall, under muscle-driven flexion, changes in strain, stress, and fluid pressure increased with increasing ICR distance, with changes in effective strains being more apparent than changes in maximum shear strains.

3.2. Predicting risk of herniation

The average effective strain in the posterolateral inner and outer AF was 0.25 and 0.26 before flexion, and no elements were predicted to fail (**Figure 9A**). Torque-driven flexion had a negligible effect on the AF effective strain, regardless of the AF location (**Figure 9A**). By contrast, muscle-driven flexion increased effective strain in both the posterolateral inner and outer AF, with the strain magnitude increasing pseudo-linearly with ICR distance (**Figure 9A**). Based on the effective strain criterion, the posterolateral outer AF was predicted to fail before the inner AF (**Figure 9A** – solid vs. hollow bars). Noticeably, the effective strain in the posterolateral outer AF reached 0.54 in Case ***I***, resulting in 65% of elements exceeding the failure threshold (**Figure 9A** – red "**+**" symbol; **Figure 9A** – Case ***I***, solid bar and circle). However, the effective strain in the posterolateral inner AF and the percentage of failed elements never exceeded 0.45 and 5% for all cases (**Figure 9A** – hollow bars and circles).

The average fiber stretch in the posterolateral inner and outer AF was 1.11 and 1.07 before flexion, and no elements were predicted to fail (**Figure 9B**). The average fiber stretch in the inner and outer AF increased pseudo-linearly with ICR distance, and failure was predicted to occur earlier in the inner AF fibers than the outer AF fibers, regardless of the type of flexion applied (**Figure 9B** – hollow vs. solid bars). For the inner AF, the

[1] Corresponding author: Grace D. O'Connell – g.oconnell@berkeley.edu

average fiber stretch was 1.21 in Case ***D***, resulting in over 60% of the elements exceeding the AF fiber stretch failure threshold (**Figure 9B** – red "*****" symbol; **Figure 9B** – Case ***D***, hollow bar and circle). For the outer AF, the average fiber stretch did not reach the failure threshold until Case ***H,*** where ~50% of the elements were predicted to fail (**Figure 9B** – red "**^**" symbol; **Figure 9B** – Case ***H***, solid bar and circle).

The average effective strain in the rim was 0.55 before flexion, with only 5% of elements predicted to fail (**Figure 10A**). The average effective strain was consistent for Cases ***A*** to ***F*** and then increased pseudo-linearly with increasing ICR distance, from 0.57 in Case ***F*** to 1.63 in Case ***J*** (**Figure 10A**). Interestingly, the percentage of failed elements followed a parabolic trend, where more than 50% of rim elements failed in Cases ***A*** and ***B*** (torque-driven), as well as in Cases ***G*** to ***J*** (muscle-driven).

The average maximum shear strain in the posterolateral inner and outer AF were both 0.14 before flexion, and no elements were predicted to fail (**Figure 10B**). AF average maximum shear strain never exceeded the failure threshold, regardless of the AF anatomical region and ICR distance (**Figure 10B**).

4. Discussion

The current study used a finite element modeling approach to investigate the risk of tissue failure leading to herniation under flexion. We employed our structure-based model that was previously validated under single and combined loading conditions to evaluate multiscale disc mechanics under torque- and muscle-driven flexion. The torque-driven models intended to replicate the commonly used *in vitro* flexion testing setup with the ICRs located on the disc, while the muscle-driven models intended to replicate the

[1] Corresponding author: Grace D. O'Connell – g.oconnell@berkeley.edu

more physiologically representative flexion motions during daily activities, with the ICRs located anterior of the disc [White and Panjabi, 1990]. The risk of herniation was assessed based on posterolateral AF failure, which was considered as a major precursor for herniation. Model simulations demonstrated vastly different disc mechanics under the two flexion setups. Our findings illustrated that by shifting the instantaneous center of rotation to the anterior of the disc, the more physiologically representative muscle-driven flexion placed the disc at a higher risk for herniation through posterolateral AF failure, which is representative of clinical observations [Schroeder et al., 2016]. Under torque-driven flexion, strains were more concentrated in the rim. This finding helped explain the more commonly observed endplate junction failure *in vitro*, which contributed to the limited success researchers have had in provoking *in vitro* herniation in the past several decades [Adams and Hutton, 1983a, b; Adams and Hutton, 1985; Wilke et al., 2016; Berger-Roscher et al., 2017].

Replicating herniation *in vitro* is essential for researchers to study herniation etiology and *in vivo* failure mechanisms related to mechanical overloading. Investigating disc failure is important for understanding and assessing workplace risks (*e.g.,* factory workers) and for evaluating the performance of engineered implants [Yan et al., 2021]. Our failure criterion defined *in vitro* herniation based on both bulk AF strain and AF fiber stretch in the posterolateral region. Under torque-driven flexion, neither the bulk AF strain nor the AF fiber stretch in the posterolateral region exceeded their respective failure threshold (failed elements < 20%; **Figure 9** – Torque-driven). Thus, herniation through the posterolateral AF was not predicted for any torque-driven flexion cases;

[1] Corresponding author: Grace D. O'Connell – g.oconnell@berkeley.edu

however, for Cases ***A*** and ***B***, the effective strain in the rim exceeded the failure threshold while the failed element percentage exceeded 50% (**Figure 10A**), suggesting that torque-driven flexion most likely initiated failure from the endplate instead of the AF. These observations agree well with *in vitro* herniation studies, where endplate junction failure instead of herniation has been the main provoked failure mode under combined loading [Adams et al., 1983a, b; Adams and Hutton, 1985; Wilke et al., 2016; Schroeder et al., 2016; Berger-Roscher et al., 2017].

Applying more physiologically relevant muscle-driven flexion increased the likelihood of herniation through posterolateral AF (**Figures 8**, **9**). The risk of *in vitro* herniation increased greatly with ICR distance. In these cases, failure was predicted to first occur in the inner AF before the outer AF fibers and bulk AF (**Figure 9B**). These predicted failure locations were consistent with clinical observations for herniated discs [Schroeder et al., 2016]. Together with the predicted failure mode (*i.e.*, endplate junction failure) under torque-driven flexion, the predictive power of our model and the failure criterion applied were demonstrated. However, caution is still needed when interpreting these results for experimental study design such that an ICR distance that may result in unwanted endplate failure under muscle-driven flexion can be avoided. For example, Case ***H*** had similar effective strains, fiber stretches, and corresponding failed element percentages in the posterolateral AF as Case ***J***, but the average effective strain in the rim for Case ***H*** was ~40% smaller (**Figure 10A**), which reduced the risk of premature rim failure and made it a more preferred option than Case ***J***.

[1] Corresponding author: Grace D. O'Connell – g.oconnell@berkeley.edu

Interstitial fluid plays a pivotal role as a stress-bearing mechanism in hydrated soft tissues, including articular cartilage, meniscus, and the intervertebral disc [Proctor et al., 1989; Ateshian et al., 1994; Zhou et al., 2021a]. In healthy cartilage, fluid pressurization can contribute to more than 80% of the total stress. A loss of fluid pressurization, which occurs with aging and degeneration, can lead to excessive stress on the tissue solid phase, making it more susceptible to damage [Ateshian et al., 1994]. In this study, we observed that the mode of flexion had a large impact on the overall fluid contribution. Particularly, our model predicted a ~50% fluid pressurization contribution before flexion, and torque-driven flexion did not alter the relative fluid pressure contribution (~50%; **Figure 7B** – diagonal bars). However, muscle-driven flexion decreased the relative fluid contribution with ICR distance, suggesting a reduced protective role from interstitial fluid. For example, the relative fluid contribution was 15% for Case ***J***, representing a ~70% decrease compared to the pre-flexion configuration (**Figure 7B** – solid bars). The decrease in fluid contribution under muscle-driven flexion was paired with increases in joint-level solid stresses (**Figure 7A**) and AF strains (**Figure 9**), which increased the overall possibility of tissue- and joint-level failure, making the disc more susceptible to herniation.

Despite extensive research on disc joint-level failure mechanics, a consensus has not been reached regarding a failure criterion, due to challenges in observing and accurately characterizing tissue damage *in vivo* or *in situ*. In addition to the effective strain- and fiber stretch-based failure criterion applied in this study, we evaluated maximum shear strain as a potential failure criterion to predict tissue failure. AF maximum shear strains and the failed element percentage never exceeded the failure

[1] Corresponding author: Grace D. O'Connell – g.oconnell@berkeley.edu

threshold (**Figure 10B**). Thus, failure was not predicted for any loading condition, making maximum shear strain an ineffective failure criterion. By contrast, agreement between model-predicted failure location (*i.e.*, endplate for the torque-driven models and posterolateral AF for the muscle-driven models) with *in vitro* and clinical observations demonstrated the predictive power of our current failure criterion based on AF local effective strain and AF fiber stretch. Additionally, in our previous work, local effective strain was shown to be an effective and accurate predictor for bulk AF failure location with a 90% agreement between model predictions and experimental observations [Werbner et al., 2017]. *In vitro* experiments replicating the torque- and muscle-driven models will be the immediate next step to fully validate the accuracy and robustness of such a failure criterion.

Axial rotation combined with flexion and axial compression has been shown to increase the risk of herniation *in vitro*; thus, it was recommended that a combination of at least these three loading modalities was applied for repeatable herniation [Veres et al., 2009, 2010; Wilke et al., 2016; Berger-Roscher et al., 2017]. We chose to not include axial rotation in this study, as the ICR location for axial rotation is a variable that also requires parametric evaluation. Interestingly, though axial rotation was not included in the loading protocol, our model predicted herniation failure through the posterolateral AF for at least three out of seven muscle-driven cases (*i.e.*, Cases ***H*** to ***J***). This could potentially make *in vitro* assessment of herniation more accessible to a wider range of researchers due to less demanding testing equipment (*i.e.*, the tester does not need to support simultaneous rotation around the transverse and sagittal axis). Furthermore, joint-level failure

[1] Corresponding author: Grace D. O'Connell – g.oconnell@berkeley.edu

mechanical tests could potentially benefit from a simpler testing protocol, as differences in mechanical test setups and protocols can introduce hard-to-identify variations in measured mechanics, making it difficult to compare data across groups [Newell et al., 2020; Costi et al., 2021].

Model predictions highlighted disparate multiscale disc mechanics, not only with different flexion setups, but with respect to different ICR locations. For example, Cases ***D*** and ***I*** were both considered muscle-driven but may represent different activities or postures (**Figure 11**). Particularly, model simulations showed large differences in bulk deformation, stress-bearing mechanisms, and intradiscal stress and strain distributions between Case ***D*** and ***I*** (**Figures 5**-**8**), resulting in differences in failure risk and failure behavior predicted (**Figures 9**, **10**). Thus, it is reasonable to assume that disc mechanics would vary considerably with ICR location under other physiologically relevant degrees of freedom, including axial rotation and lateral bending. Similar to common flexion and extension tests, most mechanical testing protocols defined the ICR on the disc for axial rotation and lateral bending [Bezci et al., 2018; Wilke et al., 2016]. Thus, by employing a similar study design framework, the current model can be further applied to investigate variations in disc mechanics under rotation and lateral bending.

One limitation to the current study was that the risk of *in vitro* herniation was only evaluated based on AF strain, AF fiber stretch, and maximum shear strain; however, previous studies have suggested that AF failure might be driven by stress [Holzapfel et al., 2005], strain energy density [Ayturk et al., 2010], or a combination of stress and strain (*i.e.*, Tsai-Wu damage criterion) [Shahraki et al., 2017]. The inclusion of a wider range of

[1] Corresponding author: Grace D. O’Connell – g.oconnell@berkeley.edu

failure criteria could further improve the robustness of model predictions, generating more accurate and precise conclusions regarding failure initiation and progression. Secondly, a welded contact was assumed between the fibers and matrix as well as between interlamellar interfaces, and other contact mechanisms were not assessed. Although the contact mechanism is not well understood, it is likely that they could change with failure initiation and progression, thus altering tissue stress and strain distributions [Bruehlmann et al., 2004; Vergari et al., 2016; Szczesny et al., 2017]. Additionally, generalized disc geometric and material properties based on measurements reported in the literature were assumed and employed in the models developed in the current study. Future studies that intend to investigate multiscale mechanics of individual discs using models of customized geometries or morphologies should consider conducting corresponding sensitivity analyses a priori to help evaluate the effect of disc geometry and material property on model predictions.

Finite element modeling provides a powerful and effective tool for assessing multiscale and multiphasic disc mechanics under loading conditions that are difficult to set up experimentally. The multiscale and multiphasic structure-based model used in this study demonstrated significant differences in mechanical behavior and risk of failure from torque- and muscle-driven flexion. Specifically, model results highlighted the effectiveness of muscle-driven flexion in provoking herniation *in vitro*. In conclusion, this study provided a potential computational framework for designing improved *in vitro* mechanical testing protocols for the intervertebral disc, which can advance the assessment of disc failure both *in vitro* and *in vivo*.

[1] Corresponding author: Grace D. O'Connell – g.oconnell@berkeley.edu

FUNDING

This work was supported by National Science Foundation (NSF) Grants 1760467 and 1751212.

[1] Corresponding author: Grace D. O’Connell – g.oconnell@berkeley.edu

REFERENCES

[1] Adam, C., Rouch, P. and Skalli, W., 2015. Inter-lamellar shear resistance confers compressive stiffness in the intervertebral disc: an image-based modelling study on the bovine caudal disc. Journal of biomechanics, 48(16), pp.4303-4308.

[2] Adams, M.A. and Hutton, W.C., 1983a. The effect of fatigue on the lumbar intervertebral disc. The Journal of bone and joint surgery. British volume, 65(2), pp.199-203.

[3] Adams, M.A. and Hutton, W.C., 1983b. The mechanics of prolapsed intervertebral disc. International orthopaedics, 6(4), pp.249-253.

[4] Adams, M.A. and Hutton, W.C., 1985. Gradual disc prolapse. Spine, 10(6), pp.524-531.

[5] Alini, M., Eisenstein, S.M., Ito, K., Little, C., Kettler, A.A., Masuda, K., Melrose, J., Ralphs, J., Stokes, I. and Wilke, H.J., 2008. Are animal models useful for studying human disc disorders/degeneration?. European Spine Journal, 17(1), pp.2-19.

[5] Amin, D.B., Moawad, C.M. and Costi, J.J., 2019. New findings confirm regional internal disc strain changes during simulation of repetitive lifting motions. Annals of biomedical engineering, 47(6), pp.1378-1390.

[6] Ateshian, G.A., Lai, W.M., Zhu, W.B. and Mow, V.C., 1994. An asymptotic solution for the contact of two biphasic cartilage layers. Journal of biomechanics, 27(11), pp.1347-1360.

[7] Ayturk, U.M., Garcia, J.J. and Puttlitz, C.M., 2010. The micromechanical role of the annulus fibrosus components under physiological loading of the lumbar spine.

[8] Barthelemy, V.M.P., Van Rijsbergen, M.M., Wilson, W., Huyghe, J.M., Van Rietbergen, B. and Ito, K., 2016. A computational spinal motion segment model incorporating a matrix composition-based model of the intervertebral disc. Journal of the mechanical behavior of biomedical materials, 54, pp.194-204.

[9] Beckstein, J.C., Sen, S., Schaer, T.P., Vresilovic, E.J. and Elliott, D.M., 2008. Comparison of animal discs used in disc research to human lumbar disc: axial compression mechanics and glycosaminoglycan content. Spine, 33(6), pp.E166-E173.

[10] Berger-Roscher, N., Casaroli, G., Rasche, V., Villa, T., Galbusera, F. and Wilke, H.J., 2017. Influence of complex loading conditions on intervertebral disc failure. Spine, 42(2), pp.E78-E85.

[1] Corresponding author: Grace D. O'Connell – g.oconnell@berkeley.edu

[11] Berg-Johansen, B., Han, M., Fields, A.J., Liebenberg, E.C., Lim, B.J., Larson, P.E., Gunduz-Demir, C., Kazakia, G.J., Krug, R. and Lotz, J.C., 2018. Cartilage endplate thickness variation measured by ultrashort echo-time MRI is associated with adjacent disc degeneration. Spine, 43(10), p.E592.

[12] Bezci, S.E., Klineberg, E.O. and O'Connell, G.D., 2018. Effects of axial compression and rotation angle on torsional mechanical properties of bovine caudal discs. Journal of the mechanical behavior of biomedical materials, 77, pp.353-359.

[13] Bezci, S.E., Werbner, B., Zhou, M., Malollari, K.G., Dorlhiac, G., Carraro, C., Streets, A. and O'Connell, G.D., 2019. Radial variation in biochemical composition of the bovine caudal intervertebral disc. JOR spine, 2(3), p.e1065.

[14] Bruehlmann, S.B., Matyas, J.R. and Duncan, N.A., 2004. ISSLS prize winner: Collagen fibril sliding governs cell mechanics in the anulus fibrosus: an in situ confocal microscopy study of bovine discs. Spine, 29(23), pp.2612-2620.

[15] Castro, A.P.G. and Alves, J.L., 2021. Numerical implementation of an osmo-poro-visco-hyperelastic finite element solver: application to the intervertebral disc. Computer Methods in Biomechanics and Biomedical Engineering, 24(5), pp.538-550.

[16] Choi, K., Kuhn, J.L., Ciarelli, M.J. and Goldstein, S.A., 1990. The elastic moduli of human subchondral, trabecular, and cortical bone tissue and the size-dependency of cortical bone modulus. Journal of biomechanics, 23(11), pp.1103-1113.

[17] Cortes, D.H., Jacobs, N.T., DeLucca, J.F. and Elliott, D.M., 2014. Elastic, permeability and swelling properties of human intervertebral disc tissues: A benchmark for tissue engineering. Journal of biomechanics, 47(9), pp.2088-2094.

[18] Costi, J.J., Ledet, E.H. and O'Connell, G.D., 2021. Spine biomechanical testing methodologies: The controversy of consensus vs scientific evidence. JOR spine, 4(1), p.e1138.

[19] Danso, E.K., Honkanen, J.T.J., Saarakkala, S. and Korhonen, R.K., 2014. Comparison of nonlinear mechanical properties of bovine articular cartilage and meniscus. Journal of biomechanics, 47(1), pp.200-206.

[20] Demers, C.N., Antoniou, J. and Mwale, F., 2004. Value and limitations of using the bovine tail as a model for the human lumbar spine. Spine, 29(24), pp.2793-2799.

[21] Ehlers, W., Karajan, N. and Markert, B., 2009. An extended biphasic model for charged hydrated tissues with application to the intervertebral disc. Biomechanics and modeling in mechanobiology, 8(3), pp.233-251.

[1] Corresponding author: Grace D. O'Connell – g.oconnell@berkeley.edu

[22] Farrell, M.D. and Riches, P.E., 2013. On the poisson's ratio of the nucleus pulposus. Journal of biomechanical engineering, 135(10), p.104501.

[23] Galbusera, F., Schmidt, H., Neidlinger-Wilke, C., Gottschalk, A. and Wilke, H.J., 2011a. The mechanical response of the lumbar spine to different combinations of disc degenerative changes investigated using randomized poroelastic finite element models. European spine journal, 20(4), pp.563-571.

[24] Galbusera, F., Schmidt, H., Neidlinger-Wilke, C. and Wilke, H.J., 2011b. The effect of degenerative morphological changes of the intervertebral disc on the lumbar spine biomechanics: a poroelastic finite element investigation. Computer methods in biomechanics and biomedical engineering, 14(8), pp.729-739.

[25] Goel, V.K., Monroe, B.T., Gilbertson, L.G. and Brinckmann, P., 1995a. Interlaminar shear stresses and laminae separation in a disc: finite element analysis of the L3-L4 motion segment subjected to axial compressive loads. Spine, 20(6), pp.689-698.

[26] Goel, V.K., Ramirez, S.A., Kong, W. and Gilbertson, L.G., 1995b. Cancellous bone Young's modulus variation within the vertebral body of a ligamentous lumbar spine—application of bone adaptive remodeling concepts.

[27] Gu, W.Y., Yao, H., Vega, A.L. and Flagler, D., 2004. Diffusivity of ions in agarose gels and intervertebral disc: effect of porosity. Annals of biomedical engineering, 32(12), pp.1710-1717.

[28] Heuer, F., Schmidt, H. and Wilke, H.J., 2008. The relation between intervertebral disc bulging and annular fiber associated strains for simple and complex loading. Journal of biomechanics, 41(5), pp.1086-1094.

[29] Holzapfel, G.A., Schulze-Bauer, C.A., Feigl, G. and Regitnig, P., 2005. Single lamellar mechanics of the human lumbar anulus fibrosus. Biomechanics and modeling in mechanobiology, 3(3), pp.125-140.

[30] Katz, J.N., 2006. Lumbar disc disorders and low-back pain: socioeconomic factors and consequences. JBJS, 88(suppl_2), pp.21-24.

[31] Kim, Y.E., Goel, V.K., Weinstein, J.N. and Lim, T.H., 1991. Effect of disc degeneration at one level on the adjacent level in axial mode. Spine, 16(3), pp.331-335.

[32] Kurowski, P. and Kubo, A.I.Z.O.H., 1986. The relationship of degeneration of the intervertebral disc to mechanical loading conditions on lumbar vertebrae. Spine, 11(7), pp.726-731.

[1] Corresponding author: Grace D. O'Connell – g.oconnell@berkeley.edu

[33] Lai, W.M., Hou, J.S. and Mow, V.C., 1991. A triphasic theory for the swelling and deformation behaviors of articular cartilage.

[34] Maas, S.A., Ellis, B.J., Ateshian, G.A. and Weiss, J.A., 2012. FEBio: finite elements for biomechanics. Journal of biomechanical engineering, 134(1).

[35] Marchand, F. and Ahmed, A.M., 1990. Investigation of the laminate structure of lumbar disc anulus fibrosus. Spine, 15(5), pp.402-410.

[36] Matcher, S.J., Winlove, C.P. and Gangnus, S.V., 2004. The collagen structure of bovine intervertebral disc studied using polarization-sensitive optical coherence tomography. Physics in Medicine & Biology, 49(7), p.1295.

[37] Michalek, A.J., Buckley, M.R., Bonassar, L.J., Cohen, I. and Iatridis, J.C., 2009. Measurement of local strains in intervertebral disc anulus fibrosus tissue under dynamic shear: contributions of matrix fiber orientation and elastin content. Journal of biomechanics, 42(14), pp.2279-2285.

[38] Newell, N., Rivera Tapia, D., Rahman, T., Lim, S., O'Connell, G.D. and Holsgrove, T.P., 2020. Influence of testing environment and loading rate on intervertebral disc compressive mechanics: An assessment of repeatability at three different laboratories. JOR spine, 3(3), p.e21110.

[39] O’Connell, G.D., Vresilovic, E.J. and Elliott, D.M., 2007a. Comparison of animals used in disc research to human lumbar disc geometry. Spine, 32(3), pp.328-333.

[40] O'Connell, G.D., Johannessen, W., Vresilovic, E.J. and Elliott, D.M., 2007b. Human internal disc strains in axial compression measured noninvasively using magnetic resonance imaging. Spine, 32(25), pp.2860-2868.

[41] Partanen, J.I., Partanen, L.J. and Vahteristo, K.P., 2017. Traceable thermodynamic quantities for dilute aqueous sodium chloride solutions at temperatures from (0 to 80) C. Part 1. Activity coefficient, osmotic coefficient, and the quantities associated with the partial molar enthalpy. Journal of Chemical & Engineering Data, 62(9), pp.2617-2632.

[42] Périé, D., Korda, D. and Iatridis, J.C., 2005. Confined compression experiments on bovine nucleus pulposus and annulus fibrosus: sensitivity of the experiment in the determination of compressive modulus and hydraulic permeability. Journal of biomechanics, 38(11), pp.2164-2171.

[43] Proctor, C.S., Schmidt, M.B., Whipple, R.R., Kelly, M.A. and Mow, V.C., 1989. Material properties of the normal medial bovine meniscus. Journal of orthopaedic research, 7(6), pp.771-782.

[1] Corresponding author: Grace D. O’Connell – g.oconnell@berkeley.edu

[44] Rohlmann, A., Zander, T., Schmidt, H., Wilke, H.J. and Bergmann, G., 2006. Analysis of the influence of disc degeneration on the mechanical behaviour of a lumbar motion segment using the finite element method. Journal of biomechanics, 39(13), pp.2484-2490.

[45] Safa, B.N., Meadows, K.D., Szczesny, S.E. and Elliott, D.M., 2017. Exposure to buffer solution alters tendon hydration and mechanics. Journal of biomechanics, 61, pp.18-25.

[46] Schmidt, H., Kettler, A., Rohlmann, A., Claes, L. and Wilke, H.J., 2007a. The risk of disc prolapses with complex loading in different degrees of disc degeneration–a finite element analysis. Clinical biomechanics, 22(9), pp.988-998.

[47] Schmidt, H., Kettler, A., Heuer, F., Simon, U., Claes, L. and Wilke, H.J., 2007b. Intradiscal pressure, shear strain, and fiber strain in the intervertebral disc under combined loading. Spine, 32(7), pp.748-755.

[48] Schmidt, H., Shirazi-Adl, A., Schilling, C. and Dreischarf, M., 2016. Preload substantially influences the intervertebral disc stiffness in loading–unloading cycles of compression. Journal of biomechanics, 49(9), pp.1926-1932.

[49] Schollum, M.L., Robertson, P.A. and Broom, N.D., 2010. How age influences unravelling morphology of annular lamellae–a study of interfibre cohesivity in the lumbar disc. Journal of anatomy, 216(3), pp.310-319.

[50] Schroeder, G.D., Guyre, C.A. and Vaccaro, A.R., 2016, March. The epidemiology and pathophysiology of lumbar disc herniations. In Seminars in Spine Surgery (Vol. 28, No. 1, pp. 2-7). WB Saunders.

[51] Shahraki, N.M., Fatemi, A., Agarwal, A. and Goel, V.K., 2017. Prediction of clinically relevant initiation and progression of tears within annulus fibrosus. Journal of Orthopaedic Research, 35(1), pp.113-122.

[52] Shen, Z.L., Dodge, M.R., Kahn, H., Ballarini, R. and Eppell, S.J., 2008. Stress-strain experiments on individual collagen fibrils. Biophysical journal, 95(8), pp.3956-3963.

[53] Shirazi-Adl, S.A., Shrivastava, S.C. and Ahmed, A.M., 1984. Stress analysis of the lumbar disc-body unit in compression. A three-dimensional nonlinear finite element study. Spine, 9(2), pp.120-134.

[54] Shirazi-Adl, A., 1992. Finite-element simulation of changes in the fluid content of human lumbar discs. Mechanical and clinical implications. Spine, 17(2), pp.206-212.

[55] Szczesny, S.E., Fetchko, K.L., Dodge, G.R. and Elliott, D.M., 2017. Evidence that interfibrillar load transfer in tendon is supported by small diameter fibrils and not

[1] Corresponding author: Grace D. O’Connell – g.oconnell@berkeley.edu

extrafibrillar tissue components. Journal of Orthopaedic Research, 35(10), pp.2127-2134.

[56] Truumees, E., 2015. A history of lumbar disc herniation from Hippocrates to the 1990s. Clinical Orthopaedics and Related Research®, 473(6), pp.1885-1895.

[57] Van Der Rijt, J.A., Van Der Werf, K.O., Bennink, M.L., Dijkstra, P.J. and Feijen, J., 2006. Micromechanical testing of individual collagen fibrils. Macromolecular bioscience, 6(9), pp.697-702.

[58] Vergari, C., Mansfield, J., Meakin, J.R. and Winlove, P.C., 2016. Lamellar and fibre bundle mechanics of the annulus fibrosus in bovine intervertebral disc. Acta biomaterialia, 37, pp.14-20.

[59] Veres, S.P., Robertson, P.A. and Broom, N.D., 2009. The morphology of acute disc herniation: a clinically relevant model defining the role of flexion. Spine, 34(21), pp.2288-2296.

[60] Veres, S.P., Robertson, P.A. and Broom, N.D., 2010. The influence of torsion on disc herniation when combined with flexion. European Spine Journal, 19(9), pp.1468-1478.

[61] Werbner, B., Zhou, M. and O'Connell, G., 2017. A novel method for repeatable failure testing of annulus fibrosus. Journal of biomechanical engineering, 139(11).

[62] Werbner, B., Spack, K. and O'Connell, G.D., 2019. Bovine annulus fibrosus hydration affects rate-dependent failure mechanics in tension. Journal of biomechanics, 89, pp.34-39.

[63] Werbner, B., Zhou, M., McMindes, N., Lee, M., Lee, A., and O'Connell, G., 2021. Saline-polyethylene glycol blends preserve in vitro annulus fibrosus hydration and mechanics: an experimental and finite-element analysis. Journal of the mechanical behavior of biomedical materials, in review.

[64] White III, A.A. and Panjabi, M.M., 1990. Clinical biomechanics of the spine.

[65] Wilke, H.J., Kienle, A., Maile, S., Rasche, V. and Berger-Roscher, N., 2016. A new dynamic six degrees of freedom disc-loading simulator allows to provoke disc damage and herniation. European Spine Journal, 25(5), pp.1363-1372.

[66] Wu, Y., Cisewski, S.E., Sachs, B.L., Pellegrini Jr, V.D., Kern, M.J., Slate, E.H. and Yao, H., 2015. The region-dependent biomechanical and biochemical properties of bovine cartilaginous endplate. Journal of biomechanics, 48(12), pp.3185-3191.

[1] Corresponding author: Grace D. O’Connell – g.oconnell@berkeley.edu

[67] Yan Y, Fan H, Li Y, Hoeglinger E, Wiesinger A, Barr A, O'Connell GD, Harris-Adamson C. Applying wearable technology and a deep learning model to predict occupational physical activities. Applied Sciences – In Press – 10/2021

[68] Yao, M., Xu, B.P., Li, Z.J., Zhu, S., Tian, Z.R., Li, D.H., Cen, J., Cheng, S.D., Wang, Y.J., Guo, Y.M. and Cui, X.J., 2020. A comparison between the low back pain scales for patients with lumbar disc herniation: validity, reliability, and responsiveness. Health and Quality of Life Outcomes, 18(1), pp.1-12.

[69] Yu, J., Tirlapur, U., Fairbank, J., Handford, P., Roberts, S., Winlove, C.P., Cui, Z. and Urban, J., 2007. Microfibrils, elastin fibres and collagen fibres in the human intervertebral disc and bovine tail disc. Journal of anatomy, 210(4), pp.460-471.

[70] Zhou, M., Bezci, S.E. and O'Connell, G.D., 2020. Multiscale composite model of fiber-reinforced tissues with direct representation of sub-tissue properties. Biomechanics and modeling in mechanobiology, 19(2), pp.745-759.

[71] Zhou, M., Lim, S. and O'Connell, G.D., 2021a. A Robust Multiscale and Multiphasic Structure-Based Modeling Framework for the Intervertebral Disc. Frontiers in Bioengineering and Biotechnology, 9, p.452.

[72] Zhou, M., Werbner, B. and O'Connell, G.D., 2021b. Fiber engagement accounts for geometry-dependent annulus fibrosus mechanics: a multiscale, Structure-Based Finite Element Study. journal of the mechanical behavior of biomedical materials, 115, p.104292.

[1] Corresponding author: Grace D. O'Connell – g.oconnell@berkeley.edu

Figure Captions List

Fig. 1 **(A)** Schematics of the multiscale bovine caudal disc motion segment model. The top inset shows the cartilage endplate geometry. The bottom right inset details the angle-ply AF fiber structure (θ: fiber angle). Radial variation of **(B)** AF fiber angle and solid volume fraction variation, and **(C)** tissue fixed charge density.

Fig. 2 **(A)** Loading schematics demonstrating the model orientation, boundary condition, and loading conditions defined in the three loading steps. **(B)** Schematic of model mid-frontal plane demonstrating the orientation and the inner and outer annulus fibrosus (AF) location. **(C)** Schematic of model mid-transverse plane demonstrating the orientation, the posterolateral region, the rim, and the locations where the AF bulging was evaluated.

Fig. 3 Schematics of **(A)** torque-driven flexion, where the instantaneous center of rotation (ICR) is located on the top bony endplate along the line of symmetry, and **(B)** muscle-driven flexion, where the ICR is located on the same anatomical transverse plane along the line of symmetry, but away from the disc. The distance between the center of the top bony endplate and the ICR was defined as the ICR distance. **(C)** The ICR location for the 10 cases investigated.

Fig. 4 The torque and force magnitudes required to achieve 5° flexion

[1] Corresponding author: Grace D. O’Connell – g.oconnell@berkeley.edu

Fig. 5 **(A)** The anterior, posterior, and average disc height at 5° flexion. The red horizontal dashed line highlights the average pre-flexion disc height. **(B)** Disc mid-frontal plane z-strain distributions for five representative cases. Anterior and posterior disc heights were labeled.

Fig. 6 **(A)** Annulus fibrosus (AF) bulging were evaluated using the post-swelling configuration as reference. Data in red and blue suggest outward and inward bulging compared to the reference configuration. **(B)** Model-predicted AF bulging after compression. Relative bulging is only shown for one side due to symmetry. **(C)** Relative bulging in the inner and outer AF evaluated in the posterior and anterior regions. Positive and negative relative bulging suggest outward and inward AF bulging compared to the reference configuration. The red horizontal dashed line represents the relative disc bulging threshold *(*0%), below which the AF was predicted to bulge inward. **(D)** Disc mid-frontal cross sections demonstrating post-flexion AF bulging for five representative cases.

Fig. 7 Model-predicted **(A)** solid stress and fluid pressure, as well as **(B)** their relative contribution to the total stress taken by the disc pre- and post-flexion*.* The red horizontal dashed line in **(B)** highlights the relative contribution before flexion.

Fig. 8 Pre- and post-flexion disc mid-frontal plane **(A)** maximum shear strain, **(B)** effective strain, **(C)** effective solid stress, and **(D)** fluid pressure

[1] Corresponding author: Grace D. O’Connell – g.oconnell@berkeley.edu

distributions for five representative cases. In the pre-flexion configuration, "*" in **(A)** and **(B)** highlight strain concentrations. Average nucleus pulposus (NP) fluid pressure was labeled in **(D)**. **(E)** Average NP fluid pressure values at 5° flexion. The red horizontal line highlights the average NP fluid pressure value before flexion.

Fig. 9 The average **(A)** effective strain and **(B)** fiber stretch with the corresponding failed element percentage evaluated in the posterolateral (post-lat) inner and outer annulus fibrosus (AF). The gray boxes represent the range where tissue failure was expected to initiate. The failed element percentage was calculated using the failure threshold highlighted by the horizontal dashed lines, above which tissue failure was highly expected. The red "*," "^," and "+" represent failure initiation in the post-lat IAF fibers, OAF fibers, and bulk OAF.

Fig. 10 **(A)** The average effective strain evaluated in the rim, and **(B)** the average maximum shear strain evaluated in the inner annulus fibrosus (AF) and outer AF in the posterolateral (post-lat) region with the corresponding failed element percentage. The gray boxes represent the range where failure was expected to initiate. The failed element percentages were calculated using the failure threshold highlighted by the horizontal dashed lines, above which tissue failure was highly expected. The red "+'s" in **(A)** represent cases with >50% failed element percentage.

[1] Corresponding author: Grace D. O'Connell – g.oconnell@berkeley.edu

Fig. 11 Disc deformation and stress-strain distribution under two physiological flexion postures. The instantaneous center of rotation (ICR) is located **(A)** close to the body, and **(B)** away from the body.

Supplementary fig. 1 Finite element meshes of individual disc components

[1] Corresponding author: Grace D. O'Connell – g.oconnell@berkeley.edu

Table Caption List

Supplementary Table 1	Triphasic material properties used in the model. NP: nucleus pulposus; AF: annulus fibrosus; CEP: cartilage endplate; φ_0: solid volume fraction; k_0: referential hydraulic permeability; M: exponential strain-dependence coefficient for permeability; E: Young's modulus; ν: Poisson's ratio; β: exponential stiffening coefficient of the Holmes–Mow model; E_{lin}: collagen fiber bundle linear-region modulus; γ: collagen fiber bundle toe-region power-law exponent; λ_0: collagen fiber bundle toe- to linear-region transitional stretch.

[1] Corresponding author: Grace D. O'Connell – g.oconnell@berkeley.edu

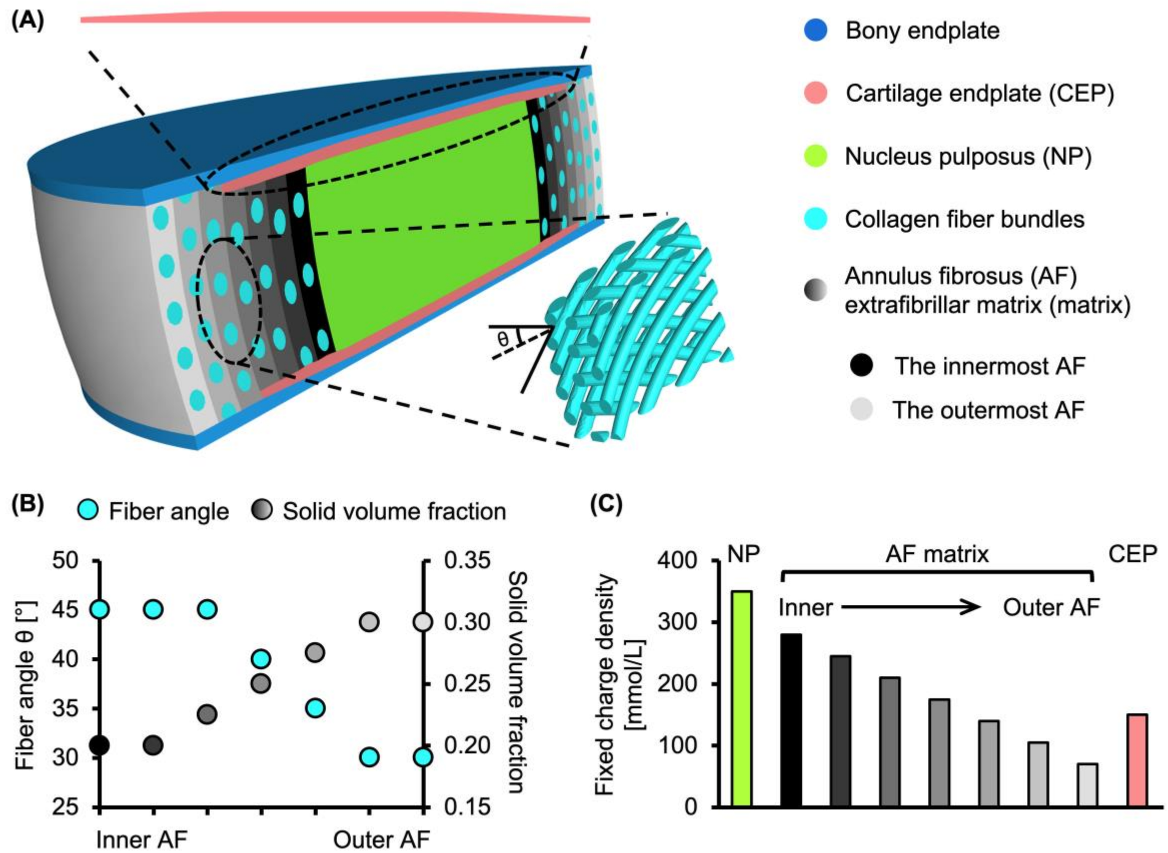

Fig. 1: (A) Schematics of the multiscale bovine caudal disc motion segment model. The top inset shows the cartilage endplate geometry. The bottom right inset details the angle-ply AF fiber structure (θ: fiber angle). Radial variation of **(B)** AF fiber angle and solid volume fraction variation, and **(C)** tissue fixed charge density.

[1] Corresponding author: Grace D. O'Connell – g.oconnell@berkeley.edu

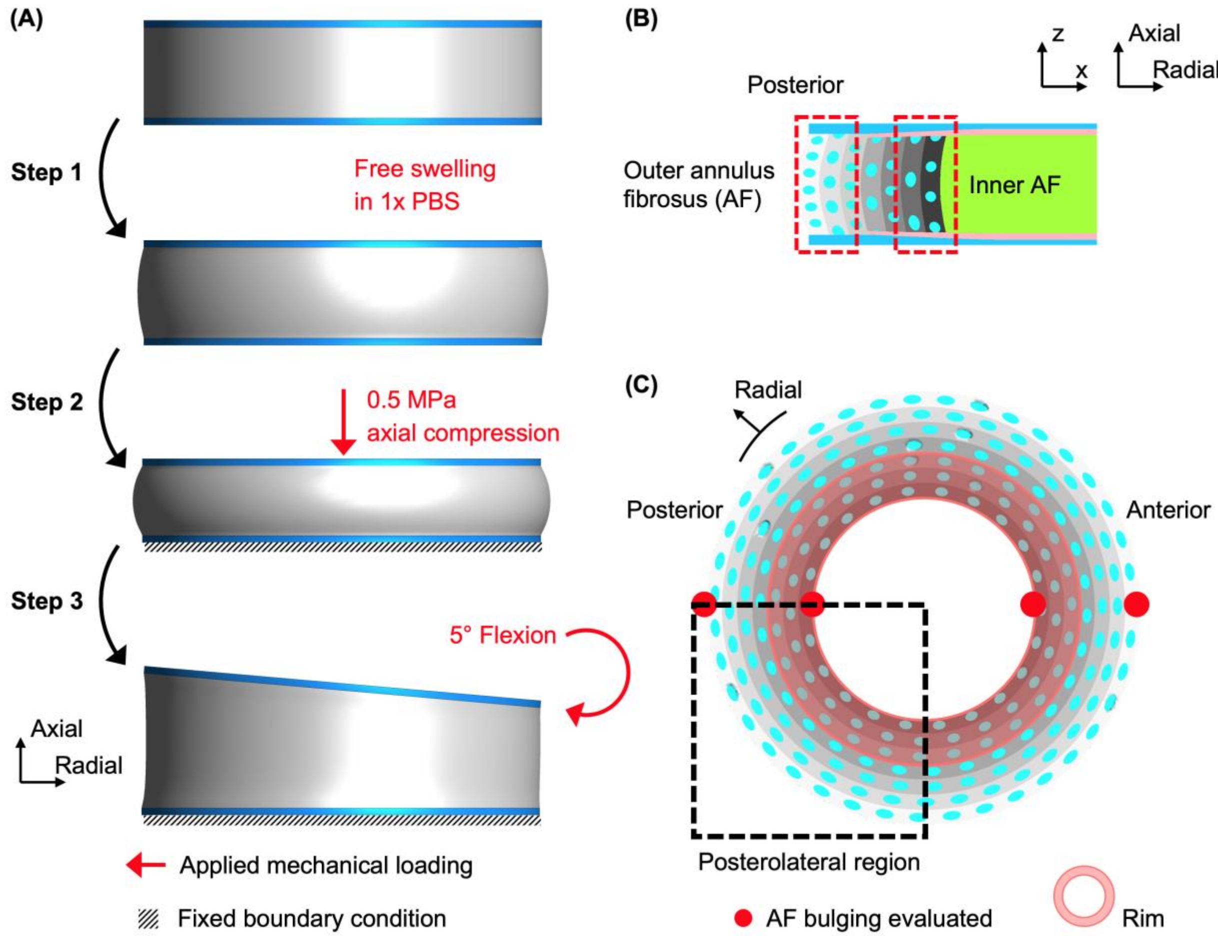

Fig. 2: (A) Loading schematics demonstrating the model orientation, boundary condition, and loading conditions defined in the three loading steps. **(B)** Schematic of model mid-frontal plane demonstrating the orientation and the inner and outer annulus fibrosus (AF) location. **(C)** Schematic of model mid-transverse plane demonstrating the orientation, the posterolateral region, the rim, and the locations where the AF bulging was evaluated.

[1] Corresponding author: Grace D. O’Connell – g.oconnell@berkeley.edu

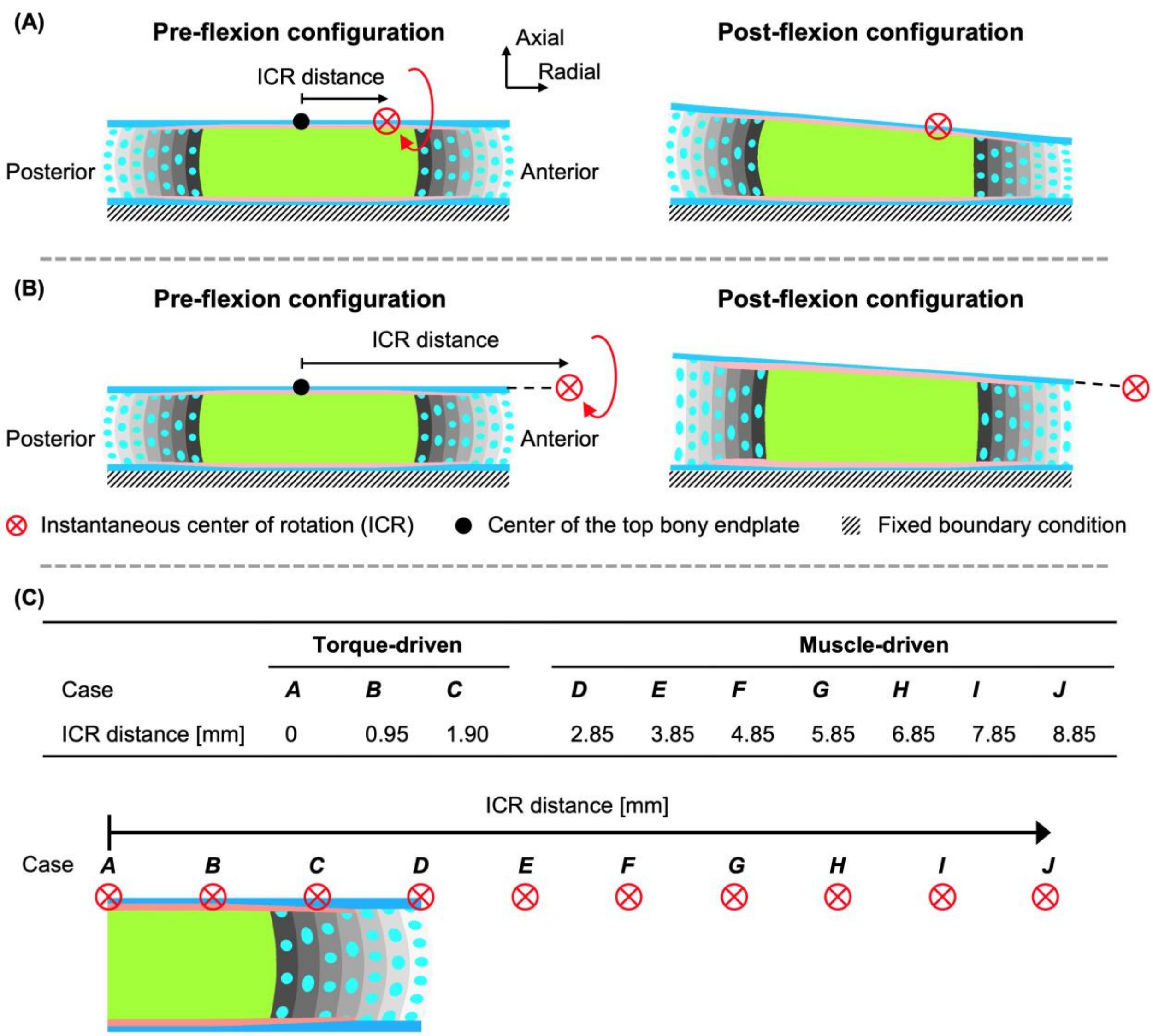

Fig. 3: Schematics of **(A)** torque-driven flexion, where the instantaneous center of rotation (ICR) is located on the top bony endplate along the line of symmetry, and **(B)** muscle-driven flexion, where the ICR is located on the same anatomical transverse plane along the line of symmetry, but away from the disc. The distance between the center of the top bony endplate and the ICR is defined as the ICR distance. **(C)** The ICR location for the 10 cases investigated.

[1] Corresponding author: Grace D. O'Connell – g.oconnell@berkeley.edu

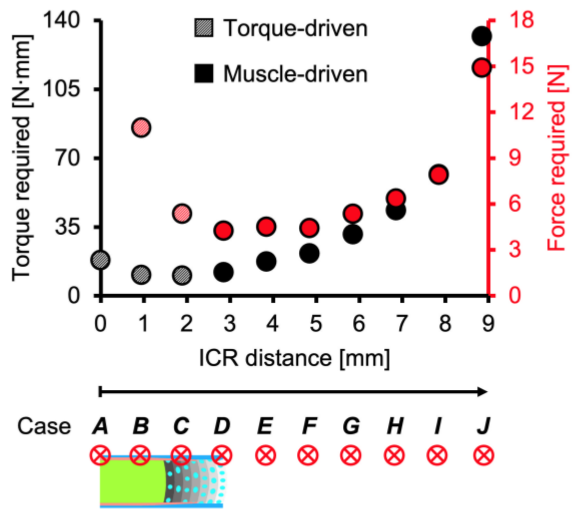

Fig. 4: The torque and force magnitudes required to achieve 5° flexion

[1] Corresponding author: Grace D. O'Connell – g.oconnell@berkeley.edu

861 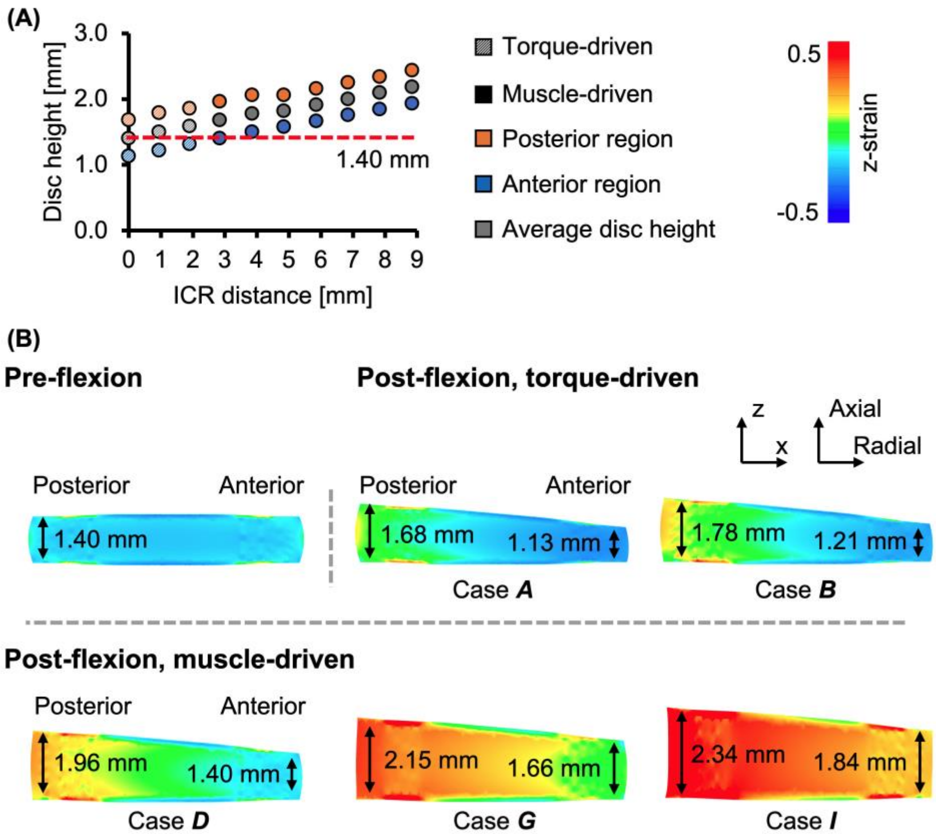

862 **Fig. 5: (A)** The anterior, posterior, and average disc height at 5° flexion. The red horizontal
863 dashed line highlights the average pre-flexion disc height. **(B)** Disc mid-frontal plane z-
864 strain distributions for five representative cases. Anterior and posterior disc heights were
865 labeled.

[1] Corresponding author: Grace D. O'Connell – g.oconnell@berkeley.edu

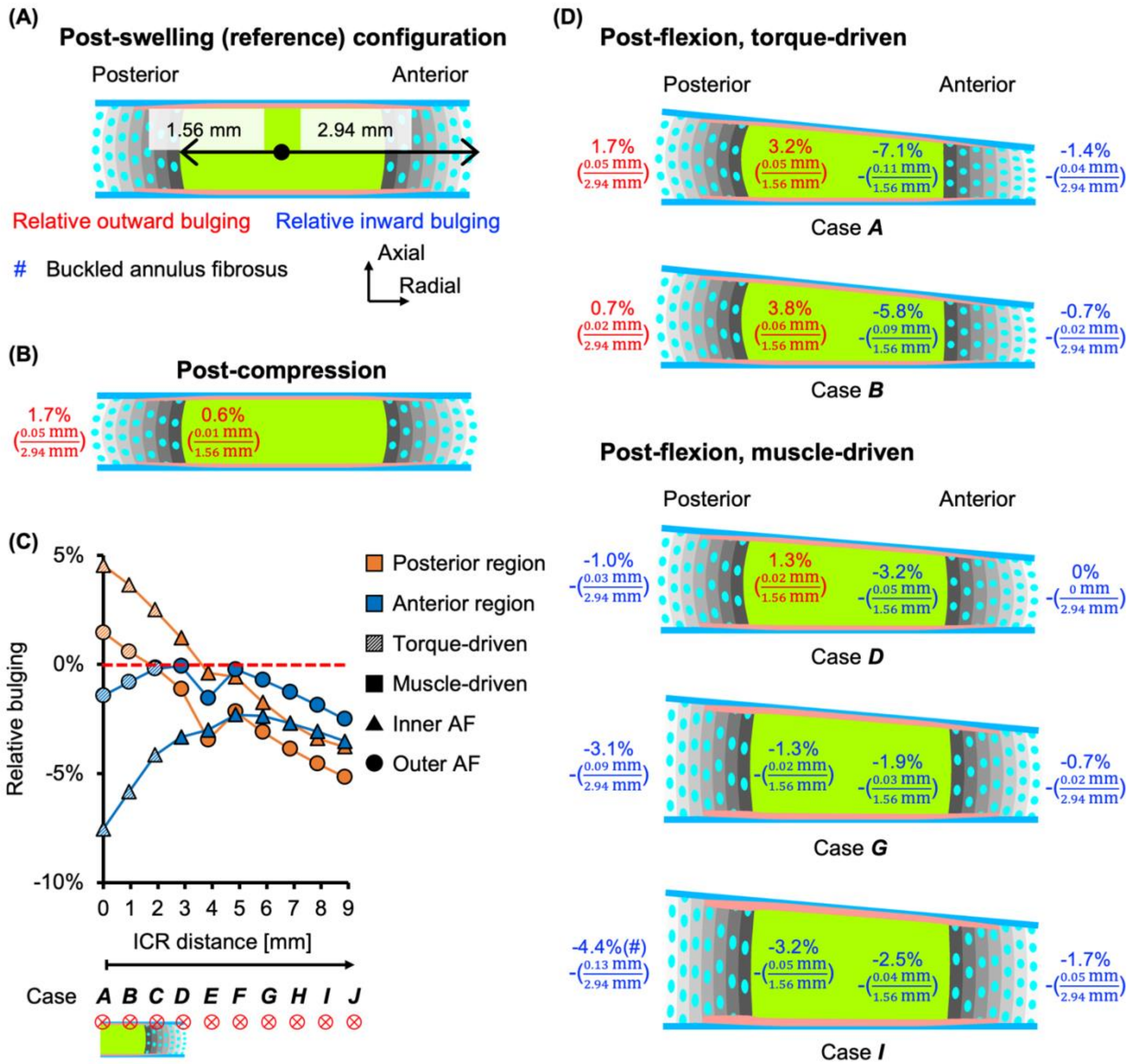

Fig. 6: (A) Annulus fibrosus (AF) bulging were evaluated using the post-swelling configuration as reference. Data in red and blue suggest outward and inward bulging compared to the reference configuration. **(B)** Model-predicted AF bulging after compression. Relative bulging is only shown for one side due to symmetry. **(C)** Relative bulging in the inner and outer AF evaluated in the posterior and anterior regions. Positive and negative relative bulging suggest outward and inward AF bulging compared to the reference configuration. The red horizontal dashed line represents the relative disc

[1] Corresponding author: Grace D. O'Connell – g.oconnell@berkeley.edu

bulging threshold *(*0%), below which the AF was predicted to bulge inward. **(D)** Disc mid-frontal cross sections demonstrating post-flexion AF bulging for five representative cases.

[1] Corresponding author: Grace D. O’Connell – g.oconnell@berkeley.edu

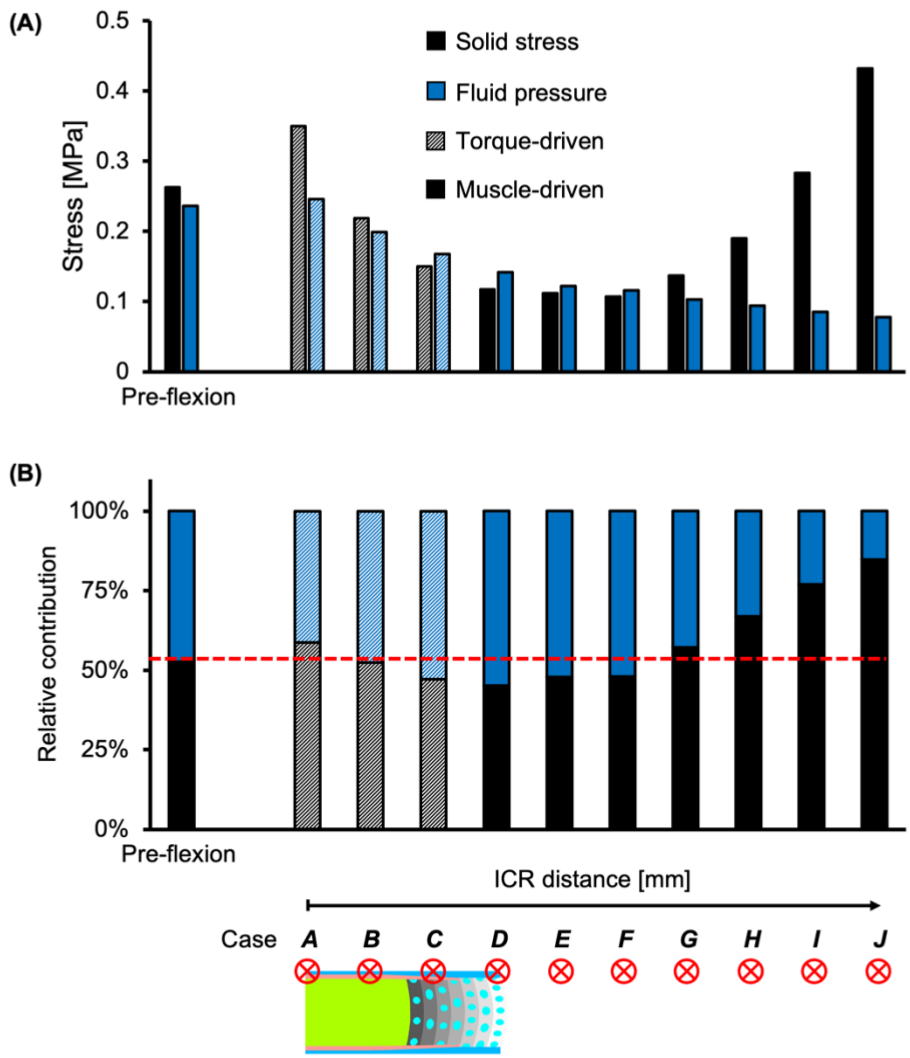

Fig. 7: Model-predicted **(A)** solid stress and fluid pressure, as well as **(B)** their relative contribution to the total stress taken by the disc pre- and post-flexion. The red horizontal dashed line in **(B)** highlights the relative contribution before flexion.

[1] Corresponding author: Grace D. O'Connell – g.oconnell@berkeley.edu

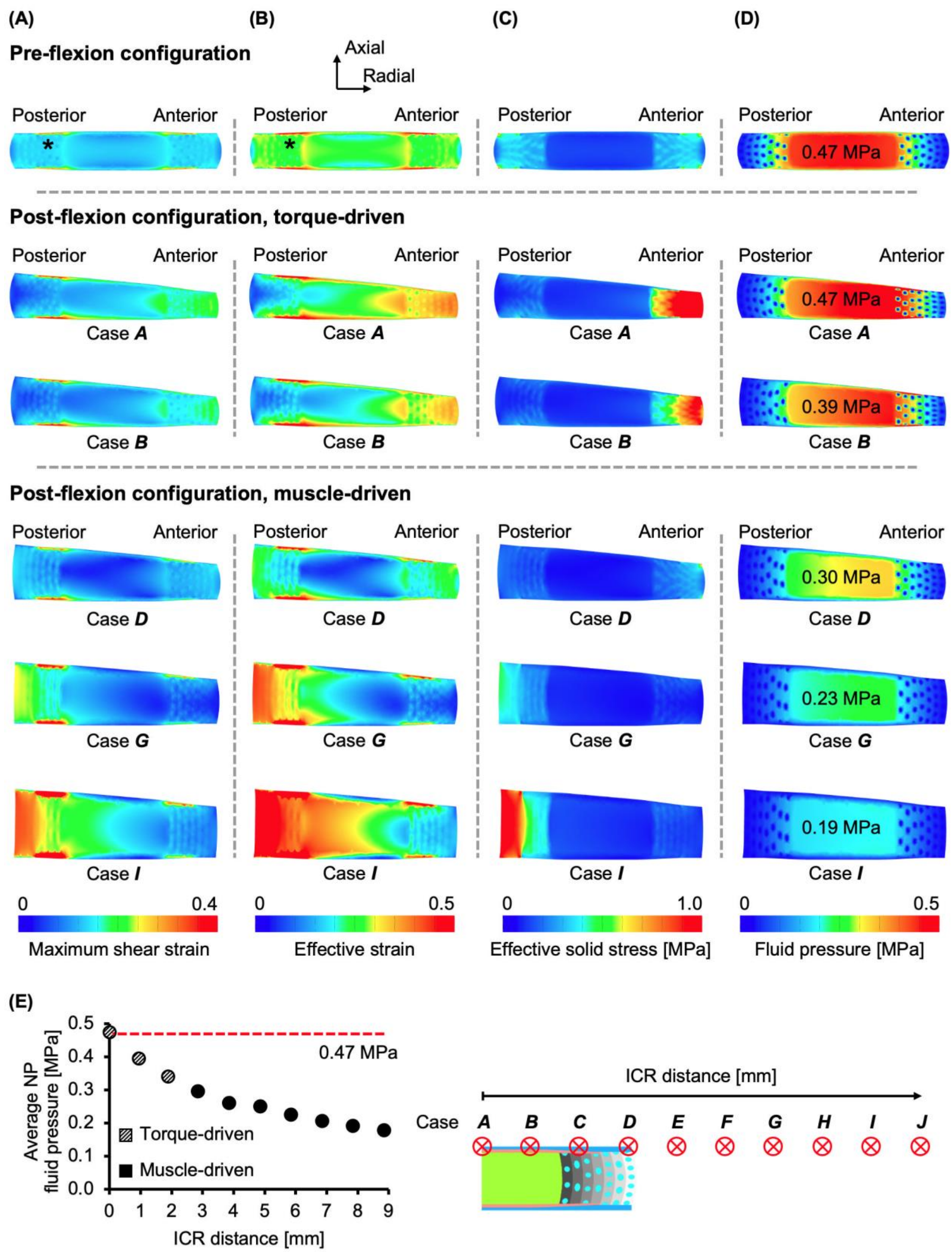

880

[1] Corresponding author: Grace D. O'Connell – g.oconnell@berkeley.edu

Fig. 8: Pre- and post-flexion disc mid-frontal plane **(A)** maximum shear strain, **(B)** effective strain, **(C)** effective solid stress, and **(D)** fluid pressure distributions for five representative cases. In the pre-flexion configuration, "*****" in **(A)** and **(B)** highlight strain concentrations. Average nucleus pulposus (NP) fluid pressure was labeled in **(D)**. **(E)** Average NP fluid pressure values at 5° flexion. The red horizontal line highlights the average NP fluid pressure value before flexion.

[1] Corresponding author: Grace D. O'Connell – g.oconnell@berkeley.edu

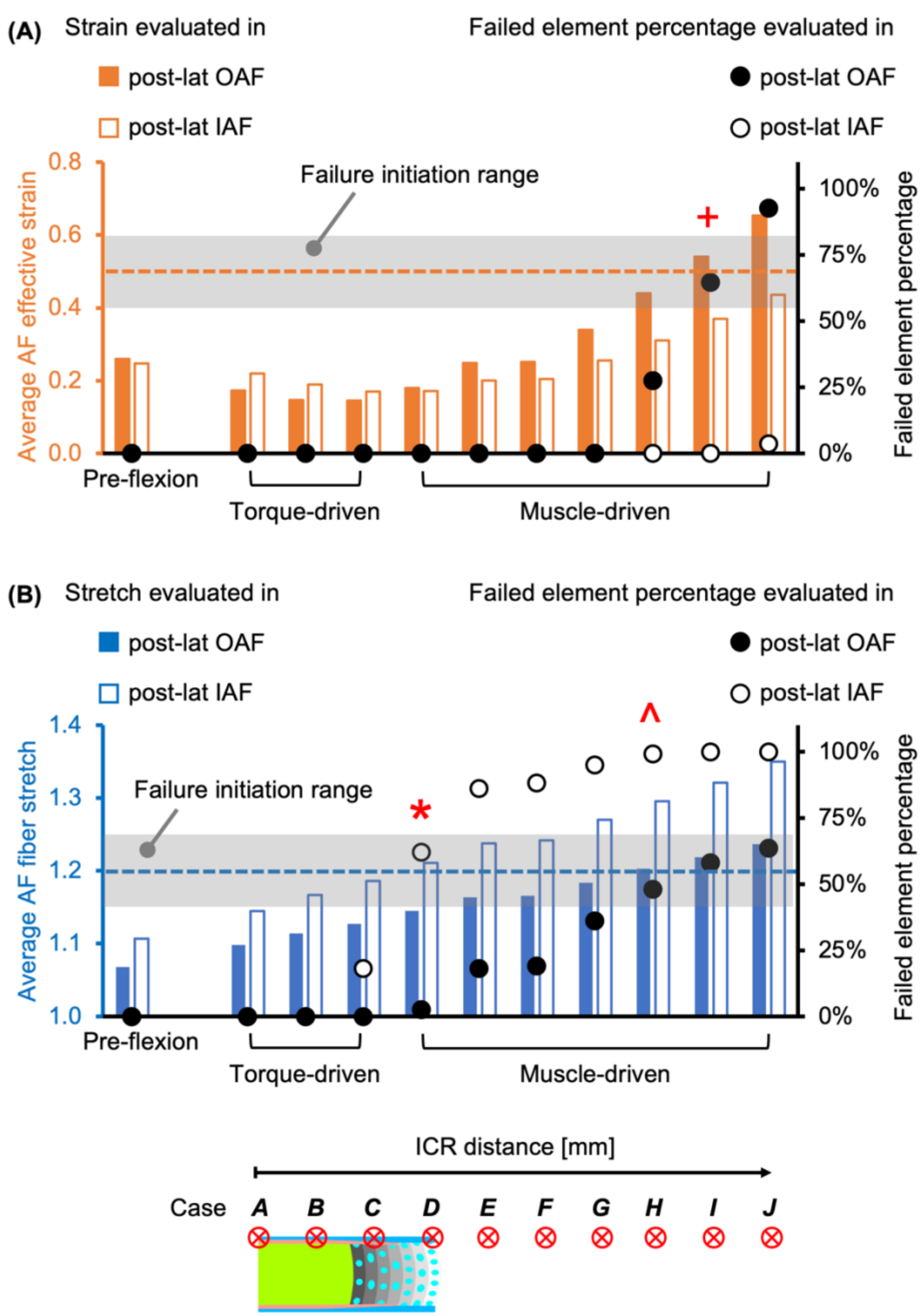

Fig. 9: The average **(A)** effective strain and **(B)** fiber stretch with the corresponding failed element percentage evaluated in the posterolateral (post-lat) inner and outer annulus fibrosus (AF). The gray boxes represent the range where tissue failure was expected to initiate. The failed element percentage was calculated using the failure threshold highlighted by the horizontal dashed lines, above which tissue failure was highly

[1] Corresponding author: Grace D. O'Connell – g.oconnell@berkeley.edu

expected. The red “*,” “^,” and “+” represent failure initiation in the post-lat IAF fibers, OAF fibers, and bulk OAF.

[1] Corresponding author: Grace D. O’Connell – g.oconnell@berkeley.edu

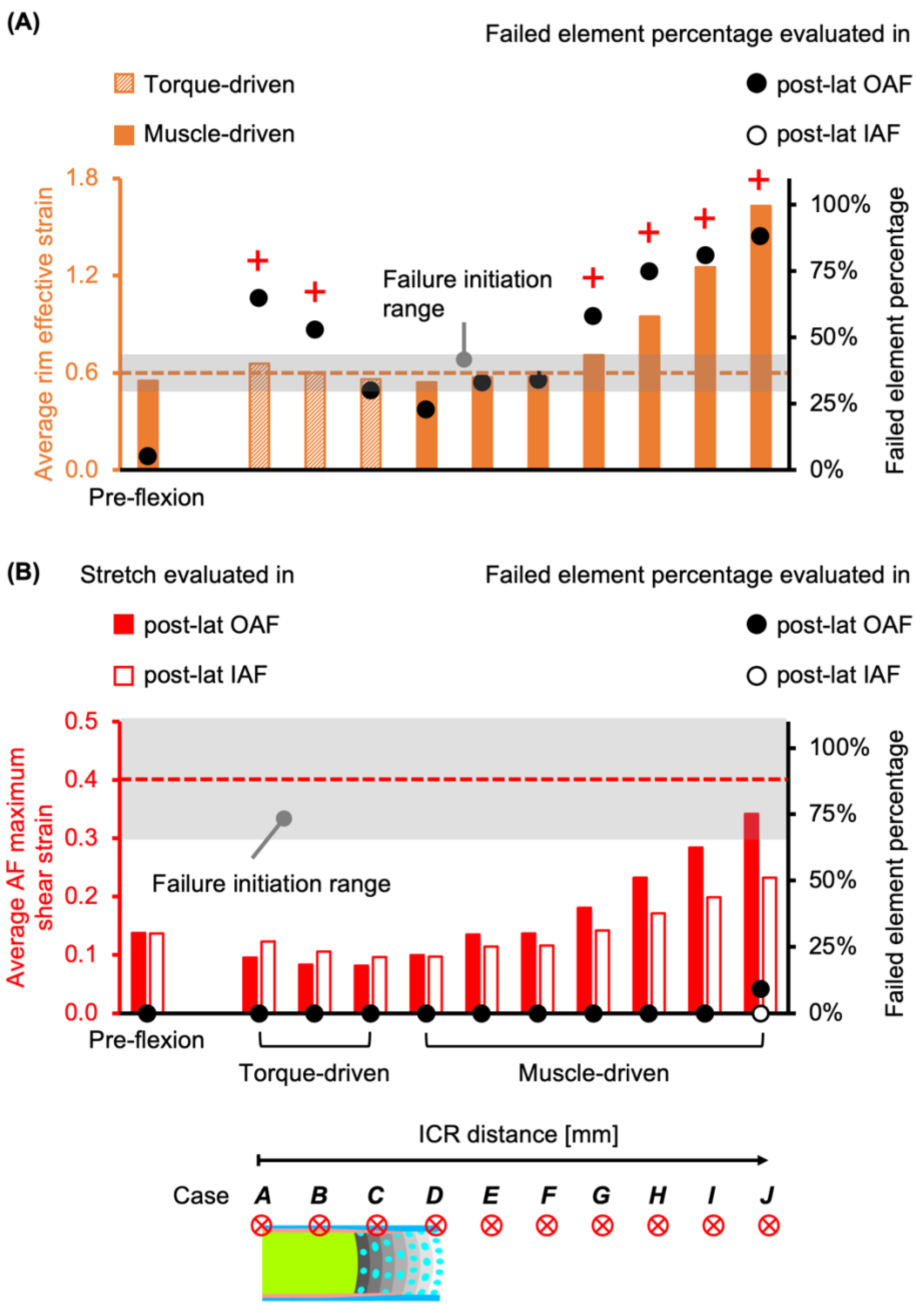

Fig. 10: (A) The average effective strain evaluated in the rim, and **(B)** the average maximum shear strain evaluated in the inner annulus fibrosus (AF) and outer AF in the posterolateral (post-lat) region with the corresponding failed element percentage. The gray boxes represent the range where failure was expected to initiate. The failed element percentages were calculated using the failure threshold highlighted by the horizontal

[1] Corresponding author: Grace D. O'Connell – g.oconnell@berkeley.edu

dashed lines, above which tissue failure was highly expected. The red “+’s” in **(A)** represent cases with >50% failed element percentage.

[1] Corresponding author: Grace D. O’Connell – g.oconnell@berkeley.edu

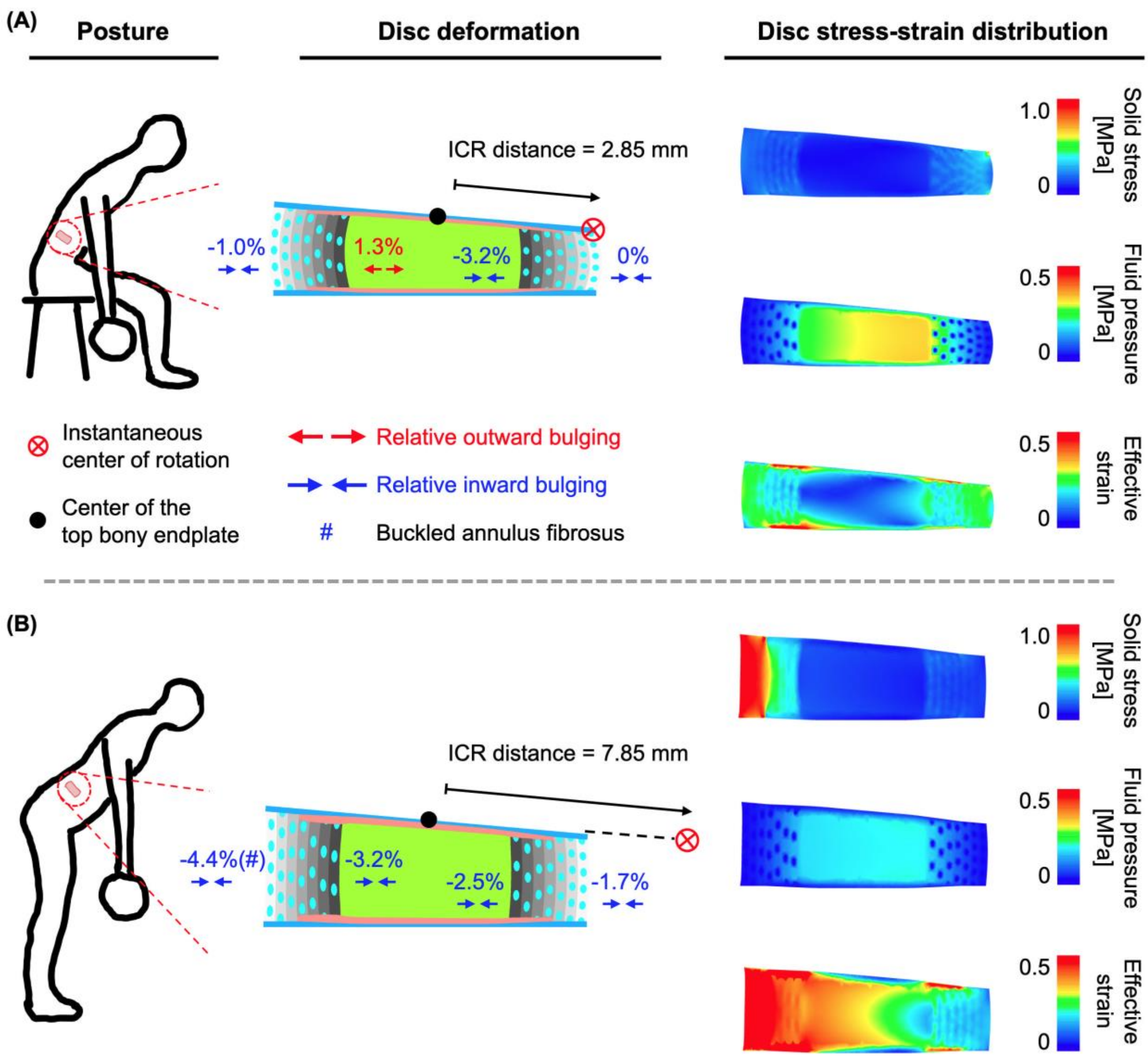

Fig. 11: Disc deformation and stress-strain distribution under two physiological flexion postures. The instantaneous center of rotation (ICR) is located **(A)** close to the body, and **(B)** away from the body.

[1] Corresponding author: Grace D. O'Connell – g.oconnell@berkeley.edu

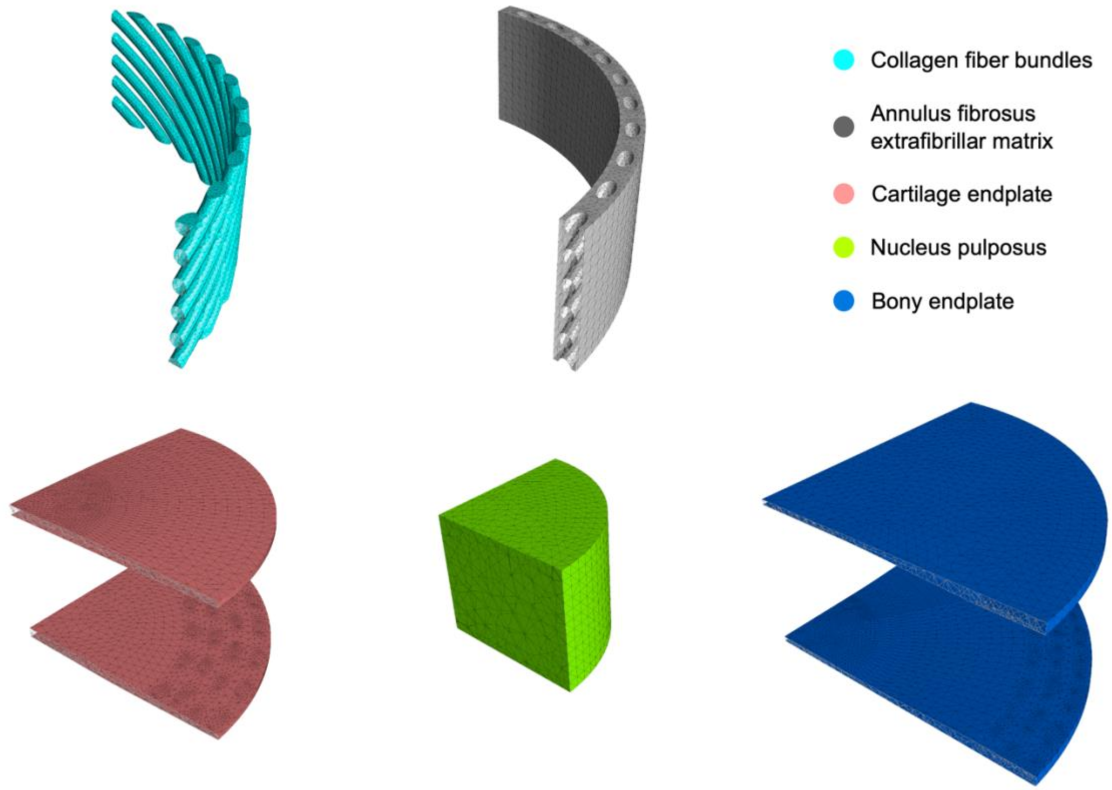

Supplementary fig. 1: Finite element meshes of individual disc components

[1] Corresponding author: Grace D. O'Connell – g.oconnell@berkeley.edu

Supplementary Table 1: Triphasic material properties used in the model. NP: nucleus pulposus; AF: annulus fibrosus; CEP: cartilage endplate; φ_0: solid volume fraction; k_0: referential hydraulic permeability; M: exponential strain-dependence coefficient for permeability; E: Young's modulus; $\boldsymbol{\nu}$: Poisson's ratio; β: exponential stiffening coefficient of the Holmes–Mow model; E_{lin}: collagen fiber bundle linear-region modulus; $\boldsymbol{\gamma}$: collagen fiber bundle toe-region power-law exponent; $\boldsymbol{\lambda_0}$: collagen fiber bundle toe- to linear-region transitional stretch.

Phase		**NP**	**AF**		**CEP**
			Matrix	**Fibers**	
Fluid	φ_0	0.2[a]	**Figure 1B**[a]		0.4[c,*]
	k_0 x 10^{-16} [m^4/Ns]	5.5[b]	64[b]	64[b]	5.6[c,*]
	M	1.92[c,*]	4.8[c,*]	4.8[c,*]	3.79[c,*]
Solid	E [MPa]	0.4[b]	0.74[b]	0.74[b]	0.31[g]
	$\boldsymbol{\nu}$	0.24[d]	0.16[c,*]	0.16[c,*]	0.18[c,*]
	$\boldsymbol{\beta}$	0.95[c,*]	3.3[c,*]	3.3[c,*]	0.29[c,*]
	E_{lin} [MPa]	N.A.	N.A.	600[e]	N.A.
	$\boldsymbol{\gamma}$	N.A.	N.A.	5.95[f,*]	N.A.
	$\boldsymbol{\lambda_0}$	N.A.	N.A.	1.05[e]	N.A.

Footnote:

*****: The parameter was determined based on experimental studies using matching human intervertebral disc tissues due to the lack of corresponding data obtained from bovine caudal disc tissues; N.A.: not applicable

[a] Beckstein et al., 2008

[b] Périé et al., 2005

[1] Corresponding author: Grace D. O'Connell – g.oconnell@berkeley.edu

[c] Cortes et al., 2014

[d] Farrell and Riches, 2013

[e] Van der Rijt et al., 2006; Shen et al., 2008

[f] Zhou et al., 2020

[g] Wu et al., 2015

[1] Corresponding author: Grace D. O’Connell – g.oconnell@berkeley.edu